

1 **Controls on the morphology of closely spaced submarine canyons**
2 **incising the continental slope of the northern South China Sea**

3
4 Jian Li ^a, Wei Li ^{a, b, *}, Tiago M. Alves ^c, Michele Rebesco^d, Xiujuan Wang^e, Shuang Li ^{a, b}, Jie Sun ^a,
5 Wenhuan Zhan ^{a, b}

6
7 ^a Key Laboratory of Ocean and Marginal Sea Geology, South China Sea Institute of Oceanology, Innovation
8 Academy of South China Sea Ecology and Environmental Engineering, Chinese Academy of Sciences, Guangzhou
9 511458, China

10 ^b University of Chinese Academy of Sciences, Beijing 100049, P.R. China

11 ^c 3D Seismic Lab. School of Earth and Ocean Sciences, Cardiff University, Main Building, Park Place, Cardiff,
12 CF10 3AT, United Kingdom

13 ^dIstituto Nazionale di Oceanografia e di Geofisica Sperimentale (OGS), Borgo Grotta Gigante 42/C, Sgonico, 34010
14 Trieste, Italy

15 ^e Key Lab of Submarine Geosciences and Prospecting Techniques, MOE, Institute for Advanced Ocean Study,
16 College of Marine Geosciences, Ocean University of China, Qingdao 266100, China

17 *Corresponding author: Dr. Wei Li (wli@scsio.ac.cn)

18
19 **Abstract**

20 Submarine canyons are key elements in source-to-sink systems that are commonly developed along
21 continental margins. They act as major conduits transferring sediment and pollutants from continental
22 shelves to deep-water basins, and control the general morphology and evolution of continental
23 margins. This work uses multibeam bathymetric and high-resolution (two- and three-dimensional)
24 seismic data to investigate the main factors controlling the morphology of the Shenhu Canyon System
25 in the northern South China Sea, as well as its detailed morphological character. The Shenhu Canyon
26 System consists of nineteen (19) submarine canyons whose morphologies vary from southwest to

27 northeast along the continental slope. Canyons (C1-C10) in the southwest show greater incision
28 depths, and steeper thalwegs and walls, when compared to their counterparts to the northeast (C11-
29 C17). The southwest canyons are located close to the shelf edge, where the upper continental slope is
30 relatively steep and multiple landslides are imaged. We show that the thalwegs and walls of the
31 southwest canyons were more actively eroded by sediment flows, with respect to the northeast
32 canyons, making them deeper and steeper. Hence, submarine canyons in the southwest, with a more
33 linear geometry, are now directly connected to the Pearl River Canyon. In parallel, seafloor fault
34 scarps act as barriers for sediment transported to the heads of the northeast canyons. This research
35 highlights how sediment supply, sediment pathways, and seafloor scarps can influence submarine
36 canyon morphology along continental slopes. It contributes to a better understanding of the factors
37 controlling canyon morphology worldwide.

38

39 **Keywords:** Seafloor morphology; Submarine canyons; Continental margin; Pearl River Mouth Basin;
40 Northern South China Sea.

41

42 **1. Introduction**

43 Submarine canyons, comprising steep-walled valleys incised onto the continental shelf and slope, can
44 form along all types of continental margin: divergent, convergent or transform (Mountjoy et al., 2009;
45 Harris and Whiteway, 2011; Puig et al., 2014). Submarine canyons have received considerable
46 attention over the last few decades as they: (1) form major conduits for sediment and pollutants
47 transported from shallow to deep marine environments (Mulder et al., 2012; Puig et al., 2013; Pope
48 et al., 2019; Zhong et al., 2021), (2) are recognised as preferential locations for gas-hydrate and
49 hydrocarbon accumulations (Mayall et al., 2006; Davies et al., 2012; Crutchley et al., 2017), and (3)

50 record climatic change with a fine-enough resolution to allow palaeoceanographic reconstructions
51 across continental margins (Zhu et al., 2010; Voigt et al., 2013).

52 Submarine canyons generally start evolving as submarine slides or slumps triggered by tectonic
53 events, high sedimentation rates, rapid delta progradation, fluid seepage or fluid overpressure
54 (Shepard, 1981; McHargue and Webb, 1986; Dugan and Flemings, 2000; Harris and Whiteway, 2011;
55 Qin et al., 2017). Their development and morphology are influenced by a number of controlling
56 factors, including sediment supply (Popescu et al., 2004; Puig et al., 2017), the eroding effect of
57 downslope sediment flows (Orange, 1999; Puga-Bernabéu et al., 2013), tectonic activity (Popescu et
58 al., 2004; Mulder et al., 2012), oceanographic currents (Mitchell, 2008; Puig et al., 2014) and even,
59 in modern times, bottom trawling and anthropogenic structures (Martin et al., 2014). Such controlling
60 factors greatly modify the morphology of submarine canyons at both their local and margin-wide
61 scales (Goff, 2001; Jobe et al., 2011; Mulder et al., 2012). Therefore, understanding the factors that
62 influence the morphology of submarine canyons can provide essential information on sediment
63 transport processes and the modern sedimentary environment as a whole (Baztan et al., 2005; Puga-
64 Bernabéu et al., 2013; Wiles et al., 2019; Naranjo-Vesga et al., 2022).

65 In recent years, an increasing number of researchers have studied the Shenhu Canyon System in the
66 northern South China Sea, which comprises nineteen (19) closely spaced submarine canyons (Zhu et
67 al., 2010; Gong et al., 2013; Ma et al., 2015; Zhou et al., 2015; Li et al., 2019; Yin et al., 2019; Su et
68 al., 2020) (Fig. 1). This was due to the discovery of deep-water hydrocarbon prospects and extensive
69 gas hydrate fields in the region (Zhu et al., 2009; Zhang et al., 2012). Previous work has addressed
70 the sub-surface geological structures (He et al., 2014; Chen et al., 2016), internal architecture (Zhu et
71 al., 2010; Gong et al., 2013; Ma et al., 2015; Zhou et al., 2015), and overall geological evolution
72 (Gong et al., 2013; Ma et al., 2015; Zhou et al., 2015) of these submarine canyons, but scant research

73 has focused on their seafloor geomorphology (e.g. Li et al., 2016; Yin et al., 2019). Significantly, the
74 submarine canyons that form the Shenhu Canyon System reveal a differing morphology along the
75 continental slope, with much steeper and more incised canyons occurring in the southwest when
76 compared with their counterparts to the northeast (Fig. 2). Even so, there is still a lack of information
77 about the factors controlling such morphological variations.

78 In this study, high-resolution bathymetric and two- and three-dimensional (2D/3D) seismic data are
79 used to investigate the Shenhu Canyon System in the northern South China Sea (Fig. 1). The specific
80 aims of this work are to: (a) quantitatively analyse the key geomorphologic features of the Shenhu
81 Canyon System and related seafloor features; (b) investigate the main factors controlling the
82 morphology of the Shenhu Canyon System; (c) discuss the effects of sediment supply, sediment
83 transport pathways, and seafloor scarps on the morphology of closely spaced submarine canyons
84 along a continental slope.

85

86 **2. Geological setting**

87 The South China Sea is a large semi-enclosed, marginal sea located at the junction between the Pacific,
88 Indian-Australian and Eurasian tectonic plates (Taylor and Hayes, 1980). Sedimentary basins
89 developing along its northern margin include, from west to east, the Yinggehai, Qiongdongnan, Pearl
90 River Mouth and Taixinan basins (Fig. 1). The Pearl River Mouth Basin, where the Shenhu Canyon
91 System is located, is the largest sedimentary basin in the northern South China Sea (Fig. 1). Its
92 evolution can be divided into two main stages (Yu, 1994): (1) early rifting and onset of tectonic
93 subsidence from Late Cretaceous to the Middle Eocene; (2) regional thermal subsidence and tilting
94 of the continental shelf, during which marine strata were accumulated from late Oligocene to the
95 present day. In addition, three main tectonic events occurred in the Pearl River Mouth Basin during

96 the Cenozoic: the Nanhai (ca. 32 Ma), Baiyun (ca. 23.8 Ma) and Dongsha (10.5 to 5.5 Ma) events
97 (Dong et al., 2009; Pang et al., 2009; Wu et al., 2014). The Dongsha tectonic event affected the
98 northeast part of the Pearl River Mouth Basin, having resulted in tectonic uplift, widespread faulting,
99 magmatic activity and local erosion (Wu et al., 2014) (Fig. 1).

100 The Shenhu Canyon System is located at a water depth between 300 m and 1700 m, and records four
101 distinct phases of evolution since 13.8 Ma (Ma et al., 2015). The heads of the submarine canyons are
102 confined to the upper continental slope, south of a broad continental shelf with an average width of
103 236 km (Huang et al., 1995). Further south, the Shenhu Canyon System joins the E-W striking Pearl
104 River Canyon, which forms one of the main conduits for sediment sourced from onshore areas into
105 deep-water basins (Figs. 1 and 2a; Ding et al., 2013). The Pearl River Delta, to the northwest of the
106 Shenhu Canyon System, has been a major source of sediment to the study area since the Late
107 Oligocene (Fig. 1; Bao, 1995; Lüdmann et al., 2001; Lin et al., 2018).

108

109 **3. Data and methods**

110 Multibeam bathymetric and high-quality 2D/3D seismic data are used in this work (Figs. 1 and 2).
111 The multibeam bathymetric data span an area of approximately 10,000 km², at a water depth of 200
112 m to 2600 m (Fig. 2a). The bathymetric data were acquired by the Guangzhou Marine Geological
113 Survey, Ministry of Land and Resources, using a SeaBeam 2112 multibeam echosounder operating
114 at a main frequency of 12 kHz with a pulse length of 3–20 ms. The raw multibeam bathymetric data
115 were post-processed using CARIS HIPS and SIPS software, so to remove noise and correct for sound
116 velocity variations within the water column. The resulting, processed bathymetric data were used to
117 generate high-resolution seabed digital terrain models (DTM) with a grid resolution of 100 m. The
118 DTMs were also used to generate slope-facing maps (aspect maps) and slope gradient maps using

119 Global Mapper®.

120 The seismic data in this work were acquired and processed by the China National Offshore Oil
121 Corporation (CNOOC) and interpreted on Kingdom® 2015 software. They were processed with a
122 sampling interval of 4 ms and a bin spacing of 25 m × 12.5 m. The frequency bandwidth of the seismic
123 data is 35-70 Hz, with a dominant frequency of 50 Hz, and their vertical resolution is ~10 m. The 2D
124 seismic profiles have a frequency bandwidth of 30-45 Hz and were sampled at a rate of 4 ms,
125 providing an average vertical resolution range between 15 m and 30 m. A water column velocity of
126 1530 m/s (Chen et al., 2016) was used to convert two-way travel time to true water depths in our
127 analysis.

128 The quantitative analysis developed in this work follows the methods of Green et al. (2007), Covault
129 et al. (2011), and Shumaker et al. (2018). A series of morphological profiles perpendicular to the
130 thalwegs were extracted from the bathymetric datasets. The profiles were computed with a spacing
131 of 50 m, decreasing to 25 m or less in areas of particular interest. In parallel, a series of longitudinal
132 profiles along the canyon thalwegs and adjacent overbanks were extracted to highlight the
133 morphological character of canyon incision. However, the data thus extracted are difficult to compare
134 and contrast because of differences in canyon length and depth. To rectify this problem, we
135 normalised the longitudinal profiles using the method in Covault et al. (2011). The canyons'
136 geomorphological parameters measured in this work include total and straight canyon length, canyon
137 sinuosity, depth of canyon incision, average canyon gradient along the canyon axis and relative to the
138 north azimuth, the distance between canyon head and shelf edge, and the gradient of the slope between
139 the canyon heads and shelf edge (Table 1).

140

141 **4. Results**

142 *4.1. Shelf edge and slope morphology in the Pearl River Mouth Basin*

143 *4.1.1. Shelf edge*

144 The shelf edge, or shelf break, is marked by an important change in slope gradient, and separates the
145 flat-lying continental shelf from a steeper slope. The exact location of the shelf edge is clear on
146 seismic profiles crossing the shelf and upper continental slope (Figs. 3 and 4b). The present-day shelf
147 edge has a depth of ~300 m in the southwest part of the study area (Fig. 3a). To the northeast, however,
148 the shelf edge occurs at a depth of ~200 m (Figs. 1 and 3). The bathymetric map of the study area
149 shows that the shelf edge generally strikes to the NE, recording an abrupt change from SE to NE at a
150 longitude of ~ 114.5°, near the southwest limit of the study area (Figs.1 and 2a).

151 Multiple shelf-edge deltas occur on the continental shelf (Figs. 3a and 4b). Seismic profiles crossing
152 the southwest sector of the study area reveal a shelf edge to upper continental slope with southeast-
153 prograding deltas, and associated clinoforms, dated as Pliocene to Quaternary in age (Ma et al., 2015;
154 Zhou et al., 2021) (Figs. 3a and 4b). Series of mass-transport deposits (MTDs) are also observed close
155 to these clinoforms (Fig. 4). The length and height of the slide scars of MTDs can be up to ~40 km
156 and ~50 m, respectively (Figs. 2a and 4). In contrast, seismic profiles crossing the upper continental
157 slope in the northeast sector of the study area reveal Pliocene-Quaternary strata as being continuous,
158 parallel or subparallel in character (Figs. 3c and 5b).

159

160 *4.1.2. Slope morphology*

161 Seismic profiles covering the continental shelf and slope of the Pearl River Mouth Basin reveal two
162 different types of continental slope (Fig. 3). Due to the presence of the Pearl River Canyon and Baiyun
163 Slide Complex downslope, seismic lines crossing the southwest part of the study area show a concave

164 slope (Figs. 3a and 3b). The continental slope is relatively steep in its upper part, where a maximum
165 gradient of $\sim 2.5^\circ$ is reached, becoming gentler towards its base (Figs. 3a and 3b). In contrast, the
166 seismic profiles crossing the northeast part of the study area reveal a convex slope with a relatively
167 gentle ($\sim 0.3^\circ$) upper slope and a steep ($\sim 2^\circ$) lower slope (Fig. 3c).

168

169 *4.2. Pearl River Canyon and linear depressions*

170 The Pearl River Canyon is sinuous in plan view and divided into three distinct reaches with differing
171 orientations (Figs. 1 and 2a). The upper reach lies on the shelf edge and upper continental slope,
172 striking to the SE (Fig. 2a). Several small-scale channels, with their heads incising the shelf edge,
173 show a V-shaped section on the upper reach, with a maximum incision depth of ~ 70 m and a width
174 of ~ 2 km (Fig. 2a). In comparison, the middle reach of the Pearl River Canyon extends for a distance
175 of ~ 80 km, changing to a predominant E-W strike at a water depth of ~ 1200 m (Fig. 2a). Lower on
176 the continental slope, at a water depth of ~ 2100 m, the general strike of the middle reach changes
177 from nearly E-W to NW-SE until one finds the continental rise (Figs. 1 and 2a). Seamounts are located
178 near the boundary between the middle and lower reaches of the Pearl River Canyon (Fig. 2a). It
179 should be noted that a giant submarine slide, the Baiyun Slide Complex, is also observed in this area
180 as shown by its prominent seabed scarp (Fig. 2a). It is the largest submarine landslide near the Pearl
181 River canyon (Fig. 2a). The Baiyun Slide Complex spans an area of ~ 11000 km², comprising multi-
182 stage overlapping submarine landslide deposits (Fig. 2a). The headwall of the Baiyun Slide Complex
183 displays an arcuate scarp, with a length of ~ 250 km and an average height of up to ~ 130 m (Figs. 2a,
184 2e and 3a).

185 Aspect maps can help to identify seafloor features with spurious strikes, highlighting the presence of
186 seafloor depressions, sidewalls, gullies and local variations in slope gradient (McAdoo, 2000).

187 Continuous and linear depressions are identified in the lower reaches of the Shenhu Canyon System
188 and Pearl River Canyon on the seafloor aspect map (Fig. 6). Their length varies from a few kilometers
189 to tens of kilometers, with a depth ranging from a few meters to tens of meters (Fig. 6). It should be
190 stressed that a series of linear depressions were developed on the canyon head in the southwest part
191 of the study area (e.g. C3-C7, C9), and some these depressions can be traced from the canyon heads
192 up to the shelf edge (e.g. C3, C4, C7) (Fig. 6b). They are up to ~1 km wide and ~100 m deep (Fig.
193 6d). However, linear depressions in the canyons to the northeast do not extend to the shelf edge. Those
194 that extend downslope from the canyon mouths are shown to bypass the seamounts, to finally enter
195 the lower reach of Pearl River Canyon (Fig. 6).

196

197 *4.3. Shenhu Canyon System*

198 *4.3.1 General geomorphology*

199 The Shenhu Canyon System consists of 19 submarine canyons, herein named C1 to C19, following
200 a southwest to northeast direction (Fig. 2a). They do not erode the shelf edge and are thus classified
201 as slope-confined canyons, with their heads located at a water depth between 350 m to 880 m (Table
202 1). Submarine canyons are 13 km to 36 km long, displaying V-shaped cross-sections in their upper
203 reaches and U-shaped cross-sections in their lower reaches (Fig. 2). The bathymetric data show they
204 are wider downslope, ranging from 2 km to 5 km in width. All these submarine canyons have no
205 obvious branches at their heads and exhibit a relatively straight thalweg with an NW-SE orientation,
206 except for C17 and C18 (Fig. 2a and Table 1). Importantly, canyons C3 to C10 can be traced into the
207 middle reach of the Pearl River Canyon, whereas the lower reaches of canyons C5 to C10 have been
208 eroded by the Baiyun Slide Complex (Fig. 2a and 2e). In the northeast part of the study area, canyons

209 C11 to C17 terminate 8 km to 50 km before reaching the Baiyun Slide Complex, though smaller-scale
210 linear depressions on their downslope prolongation still enter the lower reach of the Pearl River
211 Canyon (Figs. 2a and 6).

212

213 *4.3.2. Morphological analysis of submarine canyons*

214 Canyons C18 and C19 in the northeast portion of Shenhu Canyon System are not fully imaged by our
215 bathymetric data (Fig. 2a). A detailed analysis of canyons C1 to C17 reveals gradual variations in
216 morphological parameters such as the water depth of canyon heads, the depth of canyon incision, the
217 average slope gradient along the canyon thalweg, and the slope gradient of the canyon walls (Table
218 1).

219 The canyon heads of C1 to C17 do not incise the shelf, lying on the upper continental slope at a water
220 depth from 350 m to 730 m (except for C8) (Table 1). In addition, the depth of the canyon heads
221 increases markedly from southwest to northeast (Fig. 7a). The canyon heads of C1 to C10 occur at
222 water depths between 350 m and 580 m (except for C8), while the heads of C11-C17 are observed at
223 a water depth ranging from 660 m to 730 m (Figs. 2a and 7a). Longitudinal profiles along the canyon
224 thalwegs shows that canyons in the southwest (e.g. C3-C7, C9-C11) have concave-upward profiles,
225 while canyons to the northeast (e.g. C12-C16) have slightly concave profiles (Fig. 8). Their maximum
226 incision depth varies from 150 m to 412 m, decreasing from southwest to northeast, except for C1
227 and C2 (Fig. 7b and Table 1). The maximum incision depth of canyons C3-C10 varies from 288 m to
228 412 m in the southwest part of the study area, while it varies from 155 m to 270 m for C11-C17, in
229 the northeast (Fig. 7b). The average slope gradient along the canyon thalwegs ranges from $\sim 1.5^\circ$ to
230 $\sim 2.3^\circ$ (Table 1) and shows a decreasing trend from southwest to northeast (Fig. 7c). Canyons C1-C10
231 in the southwest have relatively steeper canyon walls, with their maximum slope gradient reaching

232 $\sim 20^\circ$ (Fig. 9a). Canyons to the northeast (C11-C17) have wall gradients of less than $\sim 15^\circ$ (Fig. 9a).
233 The distance between canyon heads and the shelf edge varies from 1.6 km to 61 km, revealing an
234 increasing trend from southwest to northeast (Fig. 10a and Table 1). In the southwest, the distance
235 between the canyon heads and shelf edge varies from 1.6 km to 8 km (except for canyon C8) and the
236 slope gradient ranges from $\sim 1.8^\circ$ to $\sim 2.7^\circ$ (Figs. 9a and 10). However, the canyons to the northeast
237 reveal a longer distance (20-61 km) between their heads and the shelf edge (Fig. 10a). The seafloor
238 in the upper part of their heads is relatively flat, with an average slope gradient ranging from $\sim 0.4^\circ$ to
239 $\sim 1.1^\circ$ (Figs. 9a and 10b).

240 As described, the submarine canyons in the Shenhu Canyon System show morphological variations
241 that follow a southwest-northeast trend along the continental slope. The incision depth, average slope
242 gradient along the canyon thalwegs, the slope gradient of the canyon walls, and the gradient of the
243 seafloor between canyon heads and shelf edge, all decrease towards the northeast. Conversely, the
244 water depth of canyon heads, and the distance between canyon heads and the shelf edge, increase
245 towards the northeast.

246

247 *4.3.3. Evolution stages of the Shenhu Canyon System*

248 The development of the Shenhu Canyon System has been divided into multi-evolutionary phases
249 based on its internal seismic facies. Seismic profiles crossing the study area reveal that small
250 individual canyons were initially formed in the Middle Miocene at ~ 13.8 Ma (Fig. 11). The size of
251 the interpreted canyons is greater, and their spacing relatively smaller, from 12.5 Ma to 10.5 Ma (Fig.
252 11). Seismic reflections show poor continuity and the presence of multiple MTDs after 10.5 Ma in
253 the northeast part of the Shenhu Canyon System, likely because the Dongsha tectonic event resulted
254 in significant basement uplift (Figs. 1 and 11). A series of small canyons were then developed in the

255 northeast part of the Shenhu Canyon System and incised upper Miocene strata data from 10.5 Ma
256 onwards (Fig. 11). However, they were completely filled and buried by younger strata, comprising
257 continuous, parallel or subparallel seismic reflections, after 5.5 Ma (Fig. 11).

258

259 *4.4 Faults and related seafloor scarps*

260 A basement high is identified on a seismic profile crossing canyons C3 to C19, with its depth below
261 the seafloor increasing to the southwest (Fig. 11). Several normal faults associated with this basement
262 high are identified on the upper continental slope (Fig. 5). Some of the faults dipping opposite to the
263 slope gradient reach the seafloor to form prominent seafloor scarps with heights of tens of meters or
264 more (Figs. 5a and 9). The high-quality bathymetry data interpreted in this work also reveals a series
265 of seafloor scarps, with lengths of 5-15 km in the northeast part of the study area (Figs. 2a and 9).
266 Faults mainly strike E-W to WNW-ESE, perpendicularly to the strike of present-day canyons (Figs.
267 2a and 9a).

268

269 **5. Discussion**

270 The geomorphological data in this work stress the important differences observed between the
271 northeast and southwest portions of the Shenhu Canyon System in terms of their incision depth, slope
272 gradient of canyon thalwegs and slope gradient of their walls (Figs. 2b, 7b, 7c and 9a). Canyons in
273 the southwest have greater incision depths, steeper canyon thalwegs, and steeper canyon walls (Figs.
274 7b, 7c and 9a). In the following sections, the factors controlling the morphology of the Shenhu
275 Canyon System are discussed.

276

277 *5.1. Canyon morphology as a function of sediment supply*

278 Shelf-edge deltas play a critical role in the partitioning and delivery of sediment to the continental
279 slope and basin floor (Gong et al., 2019; Liu et al., 2019). A deltaic succession developed on the shelf
280 edge from the Pliocene to the Quaternary in the northwest part of the study area (e.g. Bao, 1995;
281 Lüdmann et al., 2001; Lin et al., 2018; Liu et al., 2019; Wang et al., 2020) (Figs. 1, 3a and 4b). All
282 prodelta fronts reveal important progradation and, consequently, deltas have prograded onto the outer
283 shelf (Figs. 3a and 4b). Previous studies demonstrated that the Pearl River deltas have prograded 10-
284 15 km for the past 478 ky in the form of a broad sediment apron over the pre-existing shelf edge
285 (Gong et al., 2019), due to high sediment supply (Liu et al., 2019; Su et al., 2019; Wang et al., 2020).
286 Shelf-edge deltas spilling over the shelf edge can guarantee the delivery of terrestrial sediment to
287 deep-water basins regardless of relative sea-level position (Covault and Graham, 2010; Gong et al.,
288 2019).

289 In the southwest part of the study area, sediment transported by deltaic systems onto the shelf margin
290 resulted in a series of progradational, sigmoidal clinoforms (Figs. 2a, 4 and 9a). As a result of this
291 setting, the average seafloor gradient increases from $\sim 0.1^\circ$ on the shelf to $\sim 2.5^\circ$ on the upper
292 continental slope (Figs. 3a, 3b and 9a). The high sediment supply and relatively steep upper
293 continental slope promote seafloor instability and, accordingly, a series of slide scars are observed in
294 bathymetric data close to the canyon heads in the southwest (Figs. 2a, 4a and 9a). Similarly, multiple
295 MTDs are identified in between Pliocene-Quaternary clinoforms near the canyon heads (Fig. 4b).
296 Mass-wasting events originating from the shelf edge likely account for a significant portion of
297 sediment supplied to the canyons in the southwest part of the study area. In this same region,
298 information gathered from gravity and piston cores suggest a large amount of shelf-derived, coarse
299 sediment on the upper continental slope (Wang et al., 2018; Gong et al., 2019), indicating that gravity
300 flows are active (and abundant) in this region. This is consistent with the fact that longitudinal profiles

301 along the canyon thalwegs in the southwest reveal a concave-upward morphology, while canyons to
302 the northeast show a slight concave-upward geometry (Fig. 8). Such a difference is due to the fact
303 that southwest canyons have suffered relatively stronger erosion (e.g. Mitchell, 2005; Covault et al.,
304 2011). In contrast, seismic profiles crossing the upper continental slope in the northeast reveal
305 continuous, parallel or subparallel Pliocene-Quaternary strata (Figs. 3c and 5b). This shows that the
306 northeast sector of the study area is not frequently affected by mass movements (He et al., 2014; Ma
307 et al., 2015).

308 Downslope-eroding gravity flows derived from the shelf and upper continental slope, or generated
309 by downslope flow transformation of canyon-walls landslides, are common mechanisms promoting
310 axial incision in submarine canyons (Parsons et al., 2007; Rebesco et al., 2009; Puga-Bernabéu et al.,
311 2013). The walls of canyons C1-C10 in the southwest are steeper (up to $\sim 20^\circ$) than those of canyons
312 C11-C17 in the northeast (less than $\sim 15^\circ$) (Fig. 9a). Steeper canyon walls undoubtedly result in a
313 higher probability of slope instability. This is consistent with the results in Chen et al. (2016) proving
314 that the number of landslides and slumps on canyon walls decreases from southwest to northeast in
315 the study area. Downslope-eroding gravity flows generated by the unstable canyon walls are
316 considered to promote axial canyon incision (Parsons et al., 2007; Puga-Bernabéu et al., 2013).
317 Therefore, canyons in the southwest were likely eroded more frequently by gravity flows than those
318 in the northeast, promoting their greater depth and the formation of steeper thalwegs.

319

320 *5.2. Influence of sediment pathways on canyon morphology*

321 The dimension of submarine canyons is closely controlled by slope morphology (Naranjo-Vesga et
322 al., 2022). The orientation of the sediment flow pathways is controlled by the slope gradient, as these
323 flows will tend to be directed towards topographic lows (Kneller et al., 2016; Naranjo-Vesga et al.,

324 2022). The Pearl River Canyon and Shenhu Canyon System constitute the main topographic lows for
325 sediment transported from shallow to deep waters in the Pearl River Mouth Basin (Fig. 2; Ding et al.,
326 2013). Previous studies have shown that the Pearl River Canyon began its development at ~21 Ma
327 (Ding et al., 2013; Chen et al., 2020), i.e. much earlier than the Shenhu Canyon System, which started
328 to form at ~13.8 Ma (Fig. 11). After the Shenhu Canyon System was formed, it gradually became the
329 main sediment conduit on the continental slope by replacing the upper reach of the Pearl River
330 Canyon (Ding et al., 2013; Su et al., 2020). Later, the lower reaches of canyons C5 to C10 were
331 eroded by the Baiyun Slide Complex, creating prominent seafloor scarps oriented perpendicularly to
332 these canyons (Figs. 2a, 2e, 3a and 6; Li et al., 2014). The seafloor depression, or relative low,
333 generated by the Pearl River Canyon and Baiyun Slide Complex provided abundant accommodation
334 space for sediment derived from submarine canyons in the Shenhu Canyon System (Figs. 2a, 2e, 3a
335 and 6). Due to the presence of the Pearl River Canyon and Baiyun Slide Complex downslope, the
336 continental slope shows a concave-upward morphology that can be associated with the high sediment
337 supply recorded in the southwest part of the study area (Adams et al., 1998; Patruno et al., 2015; Zhuo
338 et al., 2019). Similarly, concave-upward slopes have been observed in other parts on the northern
339 South China Sea margin, such as in the Yinggehai and western Qiongdongnan basins (Zhuo et al.,
340 2019). These basins are characterised by their rapid sediment progradation, suggesting they are
341 preferential areas for sediment transport.

342 We note that the lower reaches of the southwest canyons C3-C10 are directly connected to the middle
343 reach of the Pearl River Canyon. Conversely, a series of seamounts is present between the lower
344 reaches of the northeast canyons C11-C17 and the Pearl River Canyon (Figs. 2a and 6). In addition,
345 canyons C1-C10 in the southwest are closer to the shelf edge when compared to canyons C11-C17 to
346 the northeast (Figs. 1, 2a and 10a). The distance between canyon heads and the shelf edge increases

347 significantly from southwest (~1.6 km) to northeast (61 km) (Figs. 2a, 10a and Table 1), whereas the
348 average seafloor gradient between canyon heads and the shelf edge decreases from ~2.5° to ~0.4°
349 towards the northeast (Figs. 9a and 10b). As sediment flows inevitably move downslope in the
350 direction of maximum dip, they are highly sensitive to seafloor topography and gradient (Kneller et
351 al., 2016; Naranjo-Vesga et al., 2022). This suggests that sediment flows along the shelf edge and
352 upper continental slope were more easily funneled into the canyon heads in the southwest part of the
353 study area.

354 The aspect map of the study area reveals the presence of linear depressions that are an order of
355 magnitude smaller than the submarine canyons. The linear depressions extend from the downslope
356 termination of the canyons in the Shenhu Canyon System to the middle reach of the Pearl River
357 Canyon (Fig. 6). It should be noted that some linear depressions can be traced from canyon heads to
358 the shelf edge in the southwest part of the study area (e.g. canyons C3, C4 and C7). Previous work
359 suggested that such linear depressions within canyons are troughs eroded by high-frequency sediment
360 flows (Field et al., 1999; Orange, 1999; Kneller et al., 2016; Shumaker et al., 2017; Wang et al., 2017;
361 Li et al., 2020). Once developed, such troughs are able to control the paths of sediment flows by
362 funnelling them (Normandeau et al., 2022). The distribution of linear depressions in the study area
363 illustrates that canyons in the southwest, with more linear depressions in their upslope and downslope
364 regions (Fig. 6), would have been more eroded by gravity flows. This indicates that the southwest
365 canyons, when compared with the canyons in the northeast, formed preferential pathways for
366 sediment transported from shallow to deep waters. We infer that in the area of the Shenhu Canyon
367 System, high-frequency sediment gravity flows along the depressions were sourced from larger-scale
368 canyons in the part of the slope with the highest gradient. The fact that these depressions can only be
369 traced from the canyon heads to the shelf edge in the southwest part of the study area (Fig. 6), and

370 that the southwest canyons are much deeper and steeper than those in the northeast (Figs. 7b and 7c),
371 confirms that sediment gravity flows are more active in the southwest part of the Shenhu Canyon
372 System. This also means this part of the canyon system effectively replaced the upper reaches of the
373 Pearl River Canyon in transferring sediment from shallow to deep waters (Fig. 12). This made the
374 southwest canyons much deeper and steeper than those in the northeast.

375

376 *5.3. Effect of seafloor scarps on canyon morphology*

377 Previous studies proposed tectonic uplift as a major influence on submarine canyon morphology
378 (Mountjoy et al., 2009; Harris and Whiteway, 2011; Mulder et al., 2012; Tournadour et al., 2017).

379 The most prominent example is that of submarine canyons on the northern slope of the Little Bahama
380 Bank (Mulder et al., 2012). In this region, the geometry of submarine canyons varies along a west-
381 east trending bank slope. The eastern canyons in the Little Bahama Bank are longer, deeper, wider
382 and more incised than those in the west of the bank (Mulder et al., 2012; Tournadour et al., 2017).
383 Differences in canyon morphology were considered to result from tectonic tilting of the entire
384 carbonate margin to the west during the Cenozoic (Mulder et al., 2012).

385 A series of tectonic events have occurred in and around our study area during the Cenozoic, i.e. the
386 Nanhai (ca. 32 Ma), Baiyun (ca. 23.8 Ma) and Dongsha (ca. 10.5 to 5.5 Ma) events (Dong et al., 2009;
387 Pang et al., 2009; Wu et al., 2014). Submarine canyon development in the Shenhu Canyon System
388 was largely affected by the Dongsha tectonic event (Fig. 1; Ma et al., 2015; Zhou et al., 2015), which
389 caused significant uplift in its northeast part (Figs. 3c, 5a and 11). At the time of the Dongsha tectonic
390 event, still in the northeast part of the study area, seismic reflections show poor continuity and the
391 presence of multiple MTDs (Fig. 11). This suggests the occurrence of frequent sediment flows and
392 an unstable sedimentary environment in this area. A series of smaller canyons are observed in upper

393 Miocene strata in the northeast part of the Shenhu Canyon System (Fig. 11). However, these small
394 canyons disappear in the northeast, and are replaced by continuous, parallel or subparallel seismic
395 reflections after 5.5 Ma (Fig. 11). This fact indicates that quieter open-slope conditions replaced the
396 previous sediment flows and erosion may have already ceased after 5.5 Ma in this region. In addition,
397 the present-day submarine canyons in the northeast part of the Shenhu Canyon System are smaller
398 and less incised compared to those in the southwest (Figs. 2b and 7b), and a series of seafloor scarps
399 can be observed above the canyon heads in the northeast of our study area (Figs. 3c, 5a and 9). We
400 postulate that tectonic uplift resulting from the Dongsha tectonic event does not significantly
401 influence submarine-canyon morphology at present, even though it may have played a vital role in
402 the past and may have generated the still-present rugged seafloor in the northeast of our study area
403 (Figs. 3c, 5a and 9).

404 Canyon morphology can also be affected by a rugged seafloor topography above the canyon heads
405 (Puga-Bernabéu et al., 2013). Puga-Bernabéu et al. (2013) have shown that the morphology of
406 submarine canyons varies along the Great Barrier Reef margin offshore northeastern Australia.
407 Submarine canyons with extensive barrier reefs in their upper regions are less incised and, thus, were
408 interpreted as slope-confined canyons. Conversely, submarine canyons with no well-defined barrier
409 reefs are deeply incised on the continental shelf, and sediment supply to these canyons is larger
410 compared to slope-confined canyons. Thus, the presence of barrier reefs at the shelf edge is
411 considered as one of the main factors controlling canyon morphology in the Ribbon Reef region
412 (Puga-Bernabéu et al., 2013).

413 In the study area, a series of normal faults related to local tectonic uplift are observed close to the
414 heads of canyons C16-C19 (Figs. 3c and 5). They offset the modern seafloor, resulting in the
415 formation of scarps that are up to 60 m tall (Figs. 3c, 5a and 9). These scarps are WNW-SEE striking

416 and act as physical barriers for sediment flows derived from the shelf edge (Figs. 5a, 9 and 12). The
417 root-mean-square (RMS) amplitude maps published in Ma et al., (2015) reveal obvious differences
418 on both sides of the scarps. High RMS amplitudes are located on the north side of the scarps, while
419 their southern sides show low RMS amplitudes. This implies that a large volume of coarse-grained
420 sediment is deposited on the north side of the scarps (Ma et al., 2015). The lack of seafloor scarps
421 close to the heads of canyons C1 to C15 suggests the absence of bathymetric obstacles and greater
422 sediment transport across the continental shelf and upper continental slope than those reported in Ma
423 et al. (2015) (Fig. 12). If existent, seafloor scarps would have formed physical barriers for sediment
424 transported to the canyon heads, making the northeast canyons less eroded by sediment flows.
425 The data in this work thus show that the canyons in the southwest part of the Shenhu Canyon System
426 are more incised by sediment flows than those in its northeast part, as they are closer to the Pearl
427 River delta and lack any bathymetric traps (faults scarps) for incoming sediment.

428

429 **6. Conclusions**

430 The Shenhu Canyon System of the northern South China Sea constitutes a unique case study that
431 allows us to improve our understanding on the factors controlling the morphology of closely spaced
432 submarine canyons. A combination of high-resolution bathymetric and 2D/3D seismic data were
433 therefore used in this study to investigate morphological variations in the Shenhu Canyon System of
434 the northern South China Sea. The main conclusions of this work are as follows:

435 (1) The Shenhu Canyon System consists of nineteen (19) submarine canyons showing a variable
436 morphology along the continental slope, from southwest to northeast. Canyons in the southwest have
437 greater incision depths, steeper canyon walls, and steeper thalwegs than those in the northeast.

438 (2) The differing canyon morphology observed in the study area suggests the effect of multiple

439 controlling factors, both regional and local, throughout the evolution of the Shenhu Canyon System.
440 Sediment supply, preferential pathways for sediment, and the presence of seafloor scarps, are main
441 factors controlling the morphology of the studied submarine canyons.

442 (3) Canyons C1 to C10 are close to the shelf edge, where numerous landslides occurred in the past.
443 They are connected to the Pearl River Canyon and reveal an open upper continental slope with no
444 seafloor scarps. They act as preferential pathways for sediment transported from the shelf edge into
445 the Pearl River Canyon. The canyon walls of canyons C1-C10 to the southwest are also steeper (up
446 to $\sim 20^\circ$), resulting in a higher instability of its walls. These conditions allow for higher sediment
447 supply and frequency of sediment flows, intensifying canyon erosion.

448 (4) In the northeast of the study area, the upper continental slope is characterised by a broad, low
449 gradient seafloor, probably associated with fewer sediment flows. The northeast canyons C11-C17
450 developed far from the shelf edge and have relatively gentle canyon walls ($< 15^\circ$). This makes them
451 less likely to be eroded by sediment flows sourced from the shelf edge, upper continental slope, and
452 canyon walls. In addition, seafloor scarps on the seafloor have limited the transport of sediment to
453 the Shenhu Canyon System. Consequently, the northeast canyons were less eroded by sediment flows.

454

455 **Acknowledgments**

456 We acknowledge China National Offshore Oil Corporation for their permission to release the seismic data. This
457 work was financially supported by Guangdong Basic and Applied Basic Research Foundation (No.
458 2020B1515020016), National Natural Science Foundation of China (No. 42206069), National Natural Science
459 Foundation of China (No. 41876054), Key Laboratory of Ocean and Marginal Sea Geology, Chinese Academy of
460 Sciences (No. OMG2020-09), and Guangzhou Basic and Applied Basic Research Program (No. 202201010488).
461 Dr. Wei Li is specially funded by the CAS Pioneer Hundred Talents Program (Y8SL011001). We appreciate the

462 Editor Prof. Zhongyuan Chen and three anonymous reviewers for their constructive comments, which greatly help
463 us to improve the quality of our manuscript.

464

465 **Figure and table caption**

466 Figure 1: Combined topographic and bathymetric maps of the northern South China Sea margin. The
467 orange dashed lines highlight the boundaries of four major deep-water sedimentary basins in the
468 northern half of the South China Sea. The location of the present shelf edge is indicated by the black
469 dashed line (modified from Huang et al. (2021) and Zhuo et al. (2019)). The Shenhu Canyon System
470 shown in the red box is connected with the ancient Pearl River delta (marked by the shadow in blue)
471 in the upper slope region and the Pearl River Canyon (indicated by the purple dotted line) in the
472 downslope area. The distribution of the ancient Pearl River delta is based on Bao (1995) and Lüdmann
473 et al. (2001). The area affected by Dongsha Tectonic Event is shown by the orange shadowing (Wu
474 et al., 2014).

475

476 Figure 2: (a) Bathymetry map derived from multibeam bathymetric and 3D seismic data revealing
477 the detailed seafloor morphology of Shenhu Canyon System and Pearl River Canyon. The polygons
478 with grey dotted lines represent the coverage of multibeam bathymetric data. The main sediment
479 fairway of the Pearl River Canyon is shown by a purple dashed line. The blue dashed arrows indicate
480 the locations of several submarine small-scale channels in the upper reaches of Pearl River Canyon.
481 Seafloor scarps in the northeast part of the study area are marked by black dotted lines. (b)
482 Bathymetric profile across canyons C1 to C17 showing canyon incision to decrease from southwest
483 to northeast, except for C1 and C2. (c) Bathymetric profile across the upper reach of canyons C3 to
484 C4 displaying V-shaped morphologies. (d) Bathymetric profile across the lower reach of canyons C3

485 to C4 displaying U-shaped morphologies. Note that Fig. 2c and Fig. 2d have the same horizontal and
486 vertical scales. The red lines indicate the variations of slope gradients along the bathymetric profiles
487 in Fig. 2b, 2c and 2d. (e) Three-dimensional view of the Baiyun Slide scarps highlighting the lower
488 reaches of canyons C5 to C10 as having been eroded by the Baiyun Slide.

489

490 Figure 3: (a) Two-dimensional (2D) seismic profile crossing the westernmost part of study area
491 showing the steeper upper continental slope ($\sim 2.5^\circ$) and the presence of prograding shelf-edge delta
492 and clinoform seismic facies, the shelf edge, the Baiyun Slide scarps, and the Pearl River Canyon. (b)
493 NW-SE oriented two-dimensional (2D) seismic profile depicting the slope geometry in the southwest
494 part of the Pearl River Mouth Basin. Here, the slope is generally concave and the upper continental
495 slope is steeper ($\sim 2.5^\circ$) to the lower slope ($\sim 0.7^\circ$). (c) Two-dimensional (2D) seismic profile with a
496 NW-SE orientation imaging the continental slope in the northeast part of the Pearl River Mouth Basin.
497 Here, the slope is convex with a gentle upper slope ($\sim 0.3^\circ$) and a relatively steep lower slope ($\sim 2^\circ$).
498 Note that several faults offset the seafloor to form prominent scarps. Locations of profiles are shown
499 in Fig. 1.

500

501 Figure 4: (a) Bathymetric map highlighting the detailed seafloor morphology of the shelf edge in the
502 west of study area. Note that a series of slide scars developed near the shelf edge. See Fig. 2a for
503 location. (b) Two-dimensional (2D) seismic profile crossing the upper continental slope and C9
504 showing the major depositional features, including a shelf-edge delta with clinoforms, MTDs, and
505 small submarine channels at the shelf edge to the upper continental slope. The stratigraphic
506 interpretation in this figure follows the framework of Ma et al. (2015) and Zhou et al. (2021). See Fig.
507 2a for the location of the seismic profile.

508

509 Figure 5: (a) Seismic profile from three-dimensional (3D) seismic data crossing the northeast part of
510 the Shenhu Canyon System revealing the presence of a large scarp, ~60 m high, generated when of
511 the uplift of the basement high to the NE. Faults are marked by red solid lines. See Fig. 2a for the
512 location of the seismic profile. (b) Two-dimensional (2D) seismic profile crossing the upper
513 continental slope and C16. Several faults can be observed on the upper continental slope, as marked
514 by red solid lines. Note the seismic facies replaced by continuous, parallel or subparallel seismic
515 reflections after 5.5 Ma on the upper continental slope. The stratigraphic interpretation in this figure
516 follows the framework of Ma et al. (2015).

517

518 Figure 6: (a) Slope-facing map (aspect map) of the study area derived from multibeam data. The map
519 represents the direction of slope gradient. The aspect map is important to highlight the downslope
520 trending continuous linear depressions. (b) Line-drawn interpretation of Fig. 6a revealing the wide
521 linear depressions in the study area, features that suggest significant erosion by sediment flows. The
522 white dotted arrows indicate the location of linear depressions and sediment transport pathways. (c)
523 Bathymetric profile across the continental slope revealing the presence of multiple seafloor
524 depressions. They can be up to tens of meters in depth. (d) Bathymetric profile across the upper
525 continental slope between the canyon heads and the shelf edge revealing the presence of multiple
526 seafloor depressions.

527

528 Figure 7: Variations in the morphological parameters of submarine canyons. The red dotted lines
529 highlight the variations in trend of morphological parameters. (a) The depth of canyon heads shows
530 an increasing trend from southwest to northeast, except for C8. (b) The maximum canyon incision

531 shows a decreasing trend from southwest to northeast, except for C1 and C2. (c) The average canyon
532 gradient along the axial thalwegs of submarine canyons shows a decreasing trend from southwest to
533 northeast.

534

535 Figure 8: (a) Longitudinal profiles along the canyon thalwegs of submarine canyons C1-C17. (b)
536 Normalized plots of the longitudinal profiles along the canyon thalwegs and adjacent overbanks
537 highlighting the character of canyon incision in the study area. It should be noted that canyons C4
538 and C7 in the southwest have concave-upward profiles along their thalwegs, while canyons to the
539 northeast (C12 and C15) have slightly concave profiles.

540

541 Figure 9: (a) Slope gradient map of the Shenhu Canyon System highlighting the fact that the walls of
542 canyons in the southwest (C1-C10) are steeper than those in the northeast (C11-C17). The black
543 dotted lines indicate the locations of seafloor scarps in the northeast part of the study area. (b) Three-
544 dimensional view of the slope gradient of the upper slope in the northeast part of Shenhu Canyon
545 System. Note that a series of seafloor scarps developed on the upper continental slope. (c)
546 Bathymetric profile crossing the upper continental slope revealing the presence of seafloor scarps.
547 See Fig. 9b for the location of the bathymetric profiles.

548

549 Figure 10: Variations in morphological parameters of the upper continental slope. The red dotted lines
550 highlight the variation trend of morphological parameters. (a) Distance between the canyon heads
551 and shelf edge displaying an increasing trend from southwest (~1.6 km) to northeast (~61 km). (b)
552 The average seafloor gradient between shelf edge and canyon heads shows a decreasing trend from
553 southwest (~2.1°) to northeast (~0.3°).

554

555 Figure 11: (a) Seismic profile gathered from 3D seismic data revealing the detailed internal
556 architecture of submarine canyons C3 to C19. Location of the seismic profile in Fig. 2a. The
557 development of the submarine canyons can be divided into four stages according to Ma et. al (2015).
558 Note that the significant tectonic uplift in the northeast part of the Shenhu Canyon System. (b)
559 Zoomed-in seismic section in Fig. 11a showing that the scales of submarine canyons decrease to the
560 northeast. Note that few submarine canyons can be identified in the northeast part of the Shenhu
561 Canyon System, especially above the basement high uplifted after the end of Late Miocene (5.5 Ma).

562

563 Figure 12: Three-dimensional view of a conceptual model highlighting the main sedimentary
564 processes occurring in the study area. In the southwest part of the study area, canyons are close to the
565 shelf edge where numerous landslides and sediment flows have developed. They connect with the
566 Pearl River Canyon and show an open upper continental slope lacking seafloor scarps, which act as
567 the preferential pathways for sediment transported from the shelf edge into the Pearl River Canyon.
568 In the northeast part of the study area, the upper continental slope is characterized by a broad, low-
569 gradient seafloor, with fewer sediment flows. The fault scarps act as physical barriers on the seafloor,
570 limiting the transport of sediment to the northeast canyons.

571

572 Table 1: Summary of the main characteristics of submarine canyons in the Shenhu Canyon System
573 C: canyons; HD: depth at canyon head; TD: depth at canyon end; L: total length (distance between
574 canyon head and canyon mouth measured along the canyon thalweg); SL: straight length (shortest
575 distance between canyon head and canyon mouth); S: sinuosity (ratio between the total and straight
576 length); MI: difference in maximum canyon incision depth between the canyon axis and the adjacent

577 overbanks; CGr: average canyon gradient along the canyon axes relative to horizontal; Az: azimuth
578 (orientation relative to north between the starting and ending points); D: distance between canyon
579 head and shelf edge; SGr: slope gradient of the continental slope between the canyon heads and the
580 shelf edge.

581

582 **References**

583 Adams, E.W., Schlager, W., Wattel, E., 1998. Submarine slopes with an exponential curvature. *Sedimentary Geology*
584 117, 135-141. [https://doi.org/10.1016/S0037-0738\(98\)00044-X](https://doi.org/10.1016/S0037-0738(98)00044-X).

585 Bao, C., 1995. Buried ancient channels and deltas in the Zhujiang River mouth shelf area. *Marine Geology &*
586 *Quaternary Geology* 15, 25-34 (in Chinese with English abstract). doi: 10.16562/j.cnki.0256-492.1995.02.004.

587 Baztan, J., Berné, S., Olivet, J.L., Rabineau, M., Aslanian, D., Gaudin, M., Réhault, J.P., Canals, M., 2005. Axial
588 incision: The key to understand submarine canyon evolution (in the western Gulf of Lion). *Marine and Petroleum*
589 *Geology* 22, 805-826. <https://doi.org/10.1016/j.marpetgeo.2005.03.011>.

590 Covault, J.A., Graham, S.A., 2010. Submarine fans at all sea-level stands: Tectono-morphologic and climatic
591 controls on terrigenous sediment delivery to the deep sea. *Geology* 38, 939-942. <https://doi.org/10.1130/g31081.1>.

592 Covault, J.A., Fildani, A., Romans, B.W., McHargue, T., 2011. The natural range of submarine canyon-and-channel
593 longitudinal profiles. *Geosphere* 7, 313-332. <https://doi.org/10.1130/ges00610.1>.

594 Chen, D.X., Wang, X.J., Völker, D., Wu, S.G., Wang, L., Li, W., Li, Q.P., Zhu, Z.Y., Li, C.L., Qin, Z.L., Sun, Q.L.,
595 2016. Three dimensional seismic studies of deep-water hazard-related features on the northern slope of South China
596 Sea. *Marine and Petroleum Geology* 77, 1125-1139. <https://doi.org/10.1016/j.marpetgeo.2016.08.012>.

597 Chen, H., Xie, X., Mao, K., He, Y., Su, M., Zhang, W., 2020. Depositional Characteristics and Formation
598 Mechanisms of Deep-Water Canyon Systems along the Northern South China Sea Margin. *Journal of Earth Science*
599 31, 808-819. <https://doi.org/10.1007/s12583-020-1284-z>.

600 Chen, H., Xie, X., Zhang, W., Shu, Y., Wang, D., Vandorpe, T., Van Rooij, D., 2016. Deep-water sedimentary
601 systems and their relationship with bottom currents at the intersection of Xisha Trough and Northwest Sub-Basin,
602 South China Sea. *Marine Geology* 378, 101-113. <https://doi.org/10.1016/j.margeo.2015.11.002>.

603 Crutchley, G.J., Kroeger, K.F., Pecher, I.A., Mountjoy, J.J., Gorman, A.R., 2017. Gas Hydrate Formation Amid
604 Submarine Canyon Incision: Investigations From New Zealand's Hikurangi Subduction Margin. *Geochemistry,*
605 *Geophysics, Geosystems* 18, 4299-4316. <https://doi.org/10.1002/2017gc007021>.

606 Davies, R.J., Thatcher, K.E., Mathias, S.A., Yang, J., 2012. Deepwater canyons: An escape route for methane sealed
607 by methane hydrate. *Earth and Planetary Science Letters* 323-324, 72-78. <https://doi.org/10.1016/j.epsl.2011.11.007>.

608 Ding, W., Li, J., Li, J., Fang, Y., Tang, Y., 2013. Morphotectonics and evolutionary controls on the Pearl River
609 Canyon system, South China Sea. *Marine Geophysical Research* 34, 221-238. [https://doi.org/10.1007/s11001-013-](https://doi.org/10.1007/s11001-013-9173-9)
610 [9173-9](https://doi.org/10.1007/s11001-013-9173-9).

611 Dong, D.D., Zhang, G.C., Zhong, K., Yuan, S.Q., Wu, S.G., 2009. Tectonic Evolution and Dynamics of Deepwater
612 Area of Pearl River Mouth Basin, Northern South China Sea. *Journal of Earth Science* 20, 147-159.
613 <https://doi.org/10.1007/s12583-009-0016-1>.

614 Dugan, B., Flemings, P.B., 2000. Overpressure and fluid flow in the New Jersey continental slope: Implications for
615 slope failure and cold seeps. *Science* 289, 288-291. <https://doi.org/10.1126/science.289.5477.288>.

616 Field, M.E., Gardner, J.V., Prior, D.B., 1999. Geometry and significance of stacked gullies on the northern California
617 slope. *Marine Geology* 154, 271-286. [https://doi.org/10.1016/s0025-3227\(98\)00118-2](https://doi.org/10.1016/s0025-3227(98)00118-2).

618 Goff, J.A., 2001. Quantitative classification of canyon systems on continental slopes and a possible relationship to
619 slope curvature. *Geophysical Research Letters* 28, 4359-4362. <https://doi.org/10.1029/2001gl013300>.

620 Gong, C., Steel, R.J., Wang, Y., Sweet, M.L., Xian, B., Xu, Q., Zhang, B., 2019. Shelf-edge delta overreach at the
621 shelf break can guarantee the delivery of terrestrial sediments to deep water at all sea-level stands. *Aapg Bulletin*
622 103, 65-90. <https://doi.org/10.1306/0511181617117230>.

623 Gong, C.L., Wang, Y.M., Zhu, W.L., Li, W.G., Xu, Q., 2013. Upper Miocene to Quaternary unidirectionally
624 migrating deep-water channels in the Pearl River Mouth Basin, northern South China Sea. *Aapg Bulletin* 97, 285-
625 308. <https://doi.org/10.1306/07121211159>.

626 Green, A.N., Goff, J.A., Uken, R., 2007. Geomorphological evidence for upslope canyon-forming processes on the
627 northern KwaZulu-Natal shelf, SW Indian Ocean, South Africa. *Geo-Marine Letters* 27, 399-409.
628 <https://doi.org/10.1007/s00367-007-0082-2>.

629 Harris, P.T., Whiteway, T., 2011. Global distribution of large submarine canyons: Geomorphic differences between
630 active and passive continental margins. *Marine Geology* 285, 69-86. <https://doi.org/10.1016/j.margeo.2011.05.008>.

631 He, Y., Zhong, G.F., Wang, L.L., Kuang, Z.G., 2014. Characteristics and occurrence of submarine canyon-associated
632 landslides in the middle of the northern continental slope, South China Sea. *Marine and Petroleum Geology* 57,
633 546-560. <https://doi.org/10.1016/j.marpetgeo.2014.07.003>.

634 Huang, W.K., Qiu, Y., Peng, X.C., Nie, X., Zhuo, H.T., Fu, C.G., 2021. Types and migration of shelf-breaks in the
635 central and eastern parts of the Northern South China Sea and their origin. *Marine Geology & Quaternary Geology*
636 41, 1-11 (in Chinese with English abstract). <https://doi.org/10.16562/j.cnki.0256-1492.2020060801>.

637 Huang, Z.G., Zhang, W.Q., Cai, F.X., 1995. The submerged Zhujiang Delta. *Acta Geographica Sinica* 50, 206–214
638 (in Chinese with English abstract).

639 Jobe, Z.R., Lowe, D.R., Uchytel, S.J., 2011. Two fundamentally different types of submarine canyons along the
640 continental margin of Equatorial Guinea. *Marine and Petroleum Geology* 28, 843-860.
641 <https://doi.org/10.1016/j.marpetgeo.2010.07.012>.

642 Kneller, B., Dykstra, M., Fairweather, L., Milana, J.P., 2016. Mass-transport and slope accommodation: Implications
643 for turbidite sandstone reservoirs. *Aapg Bulletin* 100, 213-235. <https://doi.org/10.1306/09011514210>.

644 Li, J., Li, W., Alves, T.M., Rebesco, M., Zhan, W., Sun, J., Mitchell, N.C., Wu, S., 2019. Different origins of seafloor
645 undulations in a submarine canyon system, northern South China Sea, based on their seismic character and relative

646 location. *Marine Geology* 413, 99-111. <https://doi.org/10.1016/j.margeo.2019.04.007>.

647 Li, W., Alves, T.M., Rebesco, M., Sun, J., Li, J., Li, S., Wu, S., 2020. The Baiyun Slide Complex, South China Sea:
648 A modern example of slope instability controlling submarine-channel incision on continental slopes. *Marine and*
649 *Petroleum Geology* 114, 104231. <https://doi.org/10.1016/j.marpetgeo.2020.104231>.

650 Li, W., Wu, S., Voelker, D., Zhao, F., Mi, L., Kopf, A., 2014. Morphology, seismic characterization and sediment
651 dynamics of the Baiyun Slide Complex on the northern South China Sea margin. *Journal of the Geological Society*
652 171, 865-877. <https://doi.org/10.1144/jgs2014-034>.

653 Li, X.S., Zhou, Q.J., Su, T.Y., Liu, L.J., Gao, S., Zhou, S.W., 2016. Slope-confined submarine canyons in the Baiyun
654 deep-water area, northern South China Sea: variation in their modern morphology. *Marine Geophysical Research*
655 37, 95-112. <https://doi.org/10.1007/s11001-016-9269-0>.

656 Lin, C., He, M., Steel, R.J., Zhang, Z., Li, H., Zhang, B., Wu, W., Shu, L., Tian, H., Zhang, X., Xing, Z., Wang, S.,
657 Zhang, M., 2018. Changes in inner- to outer-shelf delta architecture, Oligocene to Quaternary Pearl River shelf-
658 margin prism, northern South China Sea. *Marine Geology* 404, 187-204.
659 <https://doi.org/10.1016/j.margeo.2018.07.009>.

660 Liu, H.Y., Lin, C.S., Zhang, Z.T., Zhang, B., Jiang, J., Tian, H.X., Liu, H., 2019. High-resolution sequence
661 architecture and depositional evolution of the Quaternary in the northeastern shelf margin of the South China Sea.
662 *Acta Oceanologica Sinica* 38, 86-98. <https://doi.org/10.1007/s13131-019-1442-2>.

663 Lüdmann, T., Kin Wong, H., Wang, P., 2001. Plio–Quaternary sedimentation processes and neotectonics of the
664 northern continental margin of the South China Sea. *Marine Geology* 172, 331-358. [https://doi.org/10.1016/S0025-](https://doi.org/10.1016/S0025-3227(00)00129-8)
665 [3227\(00\)00129-8](https://doi.org/10.1016/S0025-3227(00)00129-8).

666 Ma, B.J., Wu, S.G., Sun, Q.L., Mi, L.J., Wang, Z.Z., Tian, J., 2015. The late Cenozoic deep-water channel system
667 in the Baiyun Sag, Pearl River Mouth Basin: Development and tectonic effects. *Deep Sea Research Part II: Topical*
668 *Studies in Oceanography* 122, 226-239. <https://doi.org/10.1016/j.dsr2.2015.06.015>.

669 Martin, J., Puig, P., Masque, P., Palanques, A., Sanchez-Gomez, A., 2014. Impact of Bottom Trawling on Deep-Sea
670 Sediment Properties along the Flanks of a Submarine Canyon. Plos One 9, e104536.
671 <https://doi.org/10.1371/journal.pone.0104536>.

672 Mayall, M., Jones, E., Casey, M., 2006. Turbidite channel reservoirs-Key elements in facies prediction and effective
673 development. Marine and Petroleum Geology 23, 821-841. <https://doi.org/10.1016/j.marpetgeo.2006.08.001>.

674 McAdoo, B.G., 2000. Mapping submarine slope failures. In: Marine and Coastal Geographical Information Systems.
675 Taylor and Francis, London, pp. 189-204.

676 McHargue, T.R., Webb, J.E., 1986. Internal geometry, seismic facies, and petroleum potential of canyons and inner
677 fan channels of the Indus Submarine Fan. Aapg Bulletin-American Association of Petroleum Geologists 70, 161–
678 180. <https://doi.org/10.1306/94885651-1704-11D7-8645000102C1865D>.

679 Mitchell, N.C., 2005. Interpreting long-profiles of canyons in the USA Atlantic continental slope. Marine Geology
680 214, 75-99. <https://doi.org/10.1016/j.margeo.2004.09.005>.

681 Mitchell, N.C., 2008. Summary of progress in geomorphologic modelling of continental slope canyons. Geological
682 Society, London, Special Publications 296, 183-194. <https://doi.org/10.1144/sp296.12>.

683 Mountjoy, J.J., Barnes, P.M., Pettinga, J.R., 2009. Morphostructure and evolution of submarine canyons across an
684 active margin: Cook Strait sector of the Hikurangi Margin, New Zealand. Marine Geology 260, 45-68.
685 <https://doi.org/10.1016/j.margeo.2009.01.006>.

686 Mulder, T., Ducassou, E., Gillet, H., Hanquiez, V., Tournadour, E., Combes, J., Eberli, G.P., Kindler, P., Gonthier,
687 E., Conesa, G., Robin, C., Sianipar, R., Reijmer, J.J.G., Francois, A., 2012. Canyon morphology on a modern
688 carbonate slope of the Bahamas: Evidence of regional tectonic tilting. Geology 40, 771-774.
689 <https://doi.org/10.1130/g33327.1>.

690 Naranjo-Vesga, J., Paniagua-Arroyave, J.F., Ortiz-Karpf, A., Jobe, Z., Wood, L., Galindo, P., Shumaker, L., Mateus-
691 Tarazona, D., 2022. Controls on submarine canyon morphology along a convergent tectonic margin. The Southern

692 Caribbean of Colombia. Marine and Petroleum Geology 137, 105493.
693 <https://doi.org/10.1016/j.marpetgeo.2021.105493>.

694 Normandeau, A., Lajeunesse, P., Ghienne, J.-F., Dietrich, P., 2022. Detailed Seafloor Imagery of Turbidity Current
695 Bedforms Reveals New Insight Into Fine-Scale Near-Bed Processes. Geophysical Research Letters 49,
696 e2021GL097389. <https://doi.org/10.1029/2021GL097389>.

697 Orange, D.L., 1999. Tectonics, sedimentation, and erosion in northern California: submarine geomorphology and
698 sediment preservation potential as a result of three competing processes. Marine Geology 154, 369-382.
699 [https://doi.org/10.1016/S0025-3227\(98\)00124-8](https://doi.org/10.1016/S0025-3227(98)00124-8).

700 Pang, X., Chen, C.M., Zhu, M., He, M., Shen, J., Lian, S.Y., Wu, X.J., Shao, L., 2009. Baiyun Movement: A
701 Significant Tectonic Event on Oligocene/Miocene Boundary in the Northern South China Sea and Its Regional
702 Implications. Journal of Earth Science 20, 49-56. <https://doi.org/10.1007/s12583-009-0005-4>.

703 Parsons, J.D., Friedrichs, C.T., Traykovski, P.A., Mohrig, D., Imran, J., Syvitski, J.P.M., Parker, G., Puig, P., Buttles,
704 J.L., Garcia, M.H., 2007. The mechanics of marine sediment gravity flows, in: Nittrouer, C.A., Austin, J.A., Field,
705 M.E., Kravitz, J.H., Syvitski, J.P.M., Wiberg, P.L. (Eds.), Continental Margin Sedimentation: From Sediment
706 Transport to Sequence Stratigraphy. Wiley-Blackwell, Hoboken, pp. 275-337.
707 <https://doi.org/10.1002/9781444304398.ch6>.

708 Patruno, S., Hampson, G.J., Jackson, C.A.L., 2015. Quantitative characterisation of deltaic and subaqueous
709 clinoforms. Earth-Science Reviews 142, 79-119. <https://doi.org/10.1016/j.earscirev.2015.01.004>.

710 Pope, E.L., Normandeau, A., Ó Cofaigh, C., Stokes, C.R., Talling, P.J., 2019. Controls on the formation of turbidity
711 current channels associated with marine-terminating glaciers and ice sheets. Marine Geology 415, 105951.
712 <https://doi.org/10.1016/j.margeo.2019.05.010>.

713 Popescu, I., Lericolais, G., Panin, N., Normand, A., Dinu, C., Le Drezen, E., 2004. The Danube submarine canyon
714 (Black Sea): morphology and sedimentary processes. Marine Geology 206, 249-265.

715 <https://doi.org/10.1016/j.margeo.2004.03.003>.

716 Puga-Bernabéu, Á., Webster, J.M., Beaman, R.J., Guilbaud, V., 2013. Variation in canyon morphology on the Great
717 Barrier Reef margin, north-eastern Australia: The influence of slope and barrier reefs. *Geomorphology* 191, 35-50.
718 <https://doi.org/10.1016/j.geomorph.2013.03.001>.

719 Puig, P., Durán, R., Muñoz, A., Elvira, E., Guillén, J., 2017. Submarine canyon-head morphologies and inferred
720 sediment transport processes in the Alías-Almanzora canyon system (SW Mediterranean): On the role of the
721 sediment supply. *Marine Geology* 393, 21-34. <https://doi.org/10.1016/j.margeo.2017.02.009>.

722 Puig, P., Greenan, B.J.W., Li, M.Z., Prescott, R.H., Piper, D.J.W., 2013. Sediment transport processes at the head of
723 Halibut Canyon, eastern Canada margin: An interplay between internal tides and dense shelf-water cascading.
724 *Marine Geology* 341, 14-28. <https://doi.org/10.1016/j.margeo.2013.05.004>.

725 Puig, P., Palanques, A., Martin, J., 2014. Contemporary Sediment-Transport Processes in Submarine Canyons, in:
726 Carlson, C.A., Giovannoni, S.J. (Eds.), *Annual Review of Marine Science*, Vol 6. Annual Reviews, Palo Alto, pp.
727 53-77. <https://doi.org/10.1146/annurev-marine-010213-135037>.

728 Qin, Yongpeng, Alves, Tiago M., Constantine, José, Gamboa, D., 2017. The Role of Mass Wasting In the Progressive
729 Development Of Submarine Channels (Espírito Santo Basin, Se Brazil). *Journal of Sedimentary Research* 87, 500-
730 516. <https://doi.org/10.2110/jsr.2017.18>.

731 Rebesco, M., Neagu, R.C., Cuppari, A., Muto, F., Accettella, D., Dominici, R., Cova, A., Romano, C., Caburlotto,
732 A., 2009. Morphobathymetric analysis and evidence of submarine mass movements in the western Gulf of Taranto
733 (Calabria margin, Ionian Sea). *International Journal of Earth Sciences* 98, 791-805. [https://doi.org/10.1007/s00531-](https://doi.org/10.1007/s00531-009-0429-1)
734 [009-0429-1](https://doi.org/10.1007/s00531-009-0429-1).

735 Shepard, F.P., 1981. Submarine Canyons: Multiple Causes and Long-Time Persistence. *Aapg Bulletin-American*
736 *Association of Petroleum Geologists* 65, 1062-1077. [https://doi.org/10.1306/03B59459-16D1-11D7-](https://doi.org/10.1306/03B59459-16D1-11D7-8645000102C1865D)
737 [8645000102C1865D](https://doi.org/10.1306/03B59459-16D1-11D7-8645000102C1865D).

738 Shumaker, L.E., Jobe, Z.R., Graham, S.A., 2017. Evolution of submarine gullies on a prograding slope: Insights
739 from 3D seismic reflection data. *Marine Geology* 393, 35-46. <https://doi.org/10.1016/j.margeo.2016.06.006>.

740 Shumaker, L.E., Jobe, Z.R., Johnstone, S.A., Pettinga, L.A., Cai, D., Moody, J.D., 2018. Controls on submarine
741 channel-modifying processes identified through morphometric scaling relationships. *Geosphere* 14, 2171-2187.
742 <https://doi.org/10.1130/ges01674.1>.

743 Su, M., Alves, T.M., Li, W., Sha, Z., Hsiung, K.-H., Liang, J., Kuang, Z., Wu, N., Zhang, B., Chiang, C.-S., 2019.
744 Reassessing two contrasting Late Miocene-Holocene stratigraphic frameworks for the Pearl River Mouth Basin,
745 northern South China Sea. *Marine and Petroleum Geology* 102, 899-913.
746 <https://doi.org/10.1016/j.marpetgeo.2018.12.034>.

747 Su, M., Lin, Z., Wang, C., Kuang, Z., Liang, J., Chen, H., Liu, S., Zhang, B., Luo, K., Huang, S., Wu, Q., 2020.
748 Geomorphologic and infilling characteristics of the slope-confined submarine canyons in the Pearl River Mouth
749 Basin, northern South China Sea. *Marine Geology* 424, 106166. <https://doi.org/10.1016/j.margeo.2020.106166>.

750 Taylor, B., Hayes, D.E., 1980. The tectonic evolution of the South China Basin. *Tectonic and Geologic Evolution*
751 *of Southeast Asian Seas and Islands* 23, 89-104. <https://doi.org/10.1029/GM023p0089>.

752 Tournadour, E., Mulder, T., Borgomano, J., Gillet, H., Chabaud, L., Ducassou, E., Hanquiez, V., Etienne, S., 2017.
753 Submarine canyon morphologies and evolution in modern carbonate settings: The northern slope of Little Bahama
754 Bank, Bahamas. *Marine Geology* 391, 76-97. <https://doi.org/10.1016/j.margeo.2017.07.014>.

755 Voigt, I., Henrich, R., Preu, B.M., Piola, A.R., Hanebuth, T.J.J., Schwenk, T., Chiessi, C.M., 2013. A submarine
756 canyon as a climate archive — Interaction of the Antarctic Intermediate Water with the Mar del Plata Canyon
757 (Southwest Atlantic). *Marine Geology* 341, 46-57. <https://doi.org/10.1016/j.margeo.2013.05.002>.

758 Wang, X., Kneller, B., Wang, Y., Chen, W., 2020. Along-strike Quaternary morphological variation of the Baiyun
759 Sag, South China Sea: The interplay between deltas, pre-existing morphology, and oceanographic processes. *Marine*
760 *and Petroleum Geology* 122, 104640. <https://doi.org/10.1016/j.marpetgeo.2020.104640>.

761 Wang, X., Zhuo, H., Wang, Y., Mao, P., He, M., Chen, W., Zhou, J., Gao, S., Wang, M., 2018. Controls of contour
762 currents on intra-canyon mixed sedimentary processes: Insights from the Pearl River Canyon, northern South China
763 Sea. *Marine Geology* 406, 193-213. <https://doi.org/10.1016/j.margeo.2018.09.016>.

764 Wang, X., Wang, Y., He, M., Chen, W., Zhuo, H., Gao, S., Wang, M., Zhou, J., 2017. Genesis and evolution of the
765 mass transport deposits in the middle segment of the Pearl River canyon, South China Sea: Insights from 3D seismic
766 data. *Marine and Petroleum Geology* 88, 555-574. <https://doi.org/10.1016/j.marpetgeo.2017.08.036>.

767 Wiles, E., Green, A., Watkeys, M., Botes, R., Jokat, W., 2019. Submarine canyons of NW Madagascar: A first
768 geomorphological insight. *Deep Sea Research Part II: Topical Studies in Oceanography* 161, 5-15.
769 <https://doi.org/10.1016/j.dsr2.2018.06.003>.

770 Wu, S., Gao, J., Zhao, S., Luedmann, T., Chen, D., Spence, G., 2014. Post-rift uplift and focused fluid flow in the
771 passive margin of northern South China Sea. *Tectonophysics* 615, 27-39.
772 <https://doi.org/10.1016/j.tecto.2013.12.013>.

773 Yin, S., Lin, L., Pope, E.L., Li, J., Ding, W., Wu, Z., Ding, W., Gao, J., Zhao, D., 2019. Continental slope-confined
774 canyons in the Pearl River Mouth Basin in the South China Sea dominated by erosion, 2004–2018. *Geomorphology*
775 344, 60-74. <https://doi.org/10.1016/j.geomorph.2019.07.016>.

776 Yu, H., Shing, 1994. Structure, stratigraphy and basin subsidence of tertiary basins along the Chinese southeastern
777 continental margin. *Tectonophysics* 235, 63-76. [https://doi.org/10.1016/0040-1951\(94\)90017-5](https://doi.org/10.1016/0040-1951(94)90017-5).

778 Zhang, G.X., Chen, F., Yang, S.X., Su, X., Sha, Z.B., Wang, H.B., Liang, J.Q., Zhou, Y., 2012. Accumulation and
779 exploration of gas hydrate in deep-sea sediments of northern South China Sea. *Chinese Journal of Oceanology and*
780 *Limnology* 30, 876-888. <https://doi.org/10.1007/s00343-012-1313-6>.

781 Zhong, G., Peng, X., 2021. Transport and accumulation of plastic litter in submarine canyons—The role of gravity
782 flows. *Geology* 49, 581-586. <https://doi.org/10.1130/g48536.1>.

783 Zhou, W., Chiarella, D., Zhuo, H., Wang, Y., Tang, W., Zou, M., Xu, Q., 2021. Genesis and evolution of large-scale

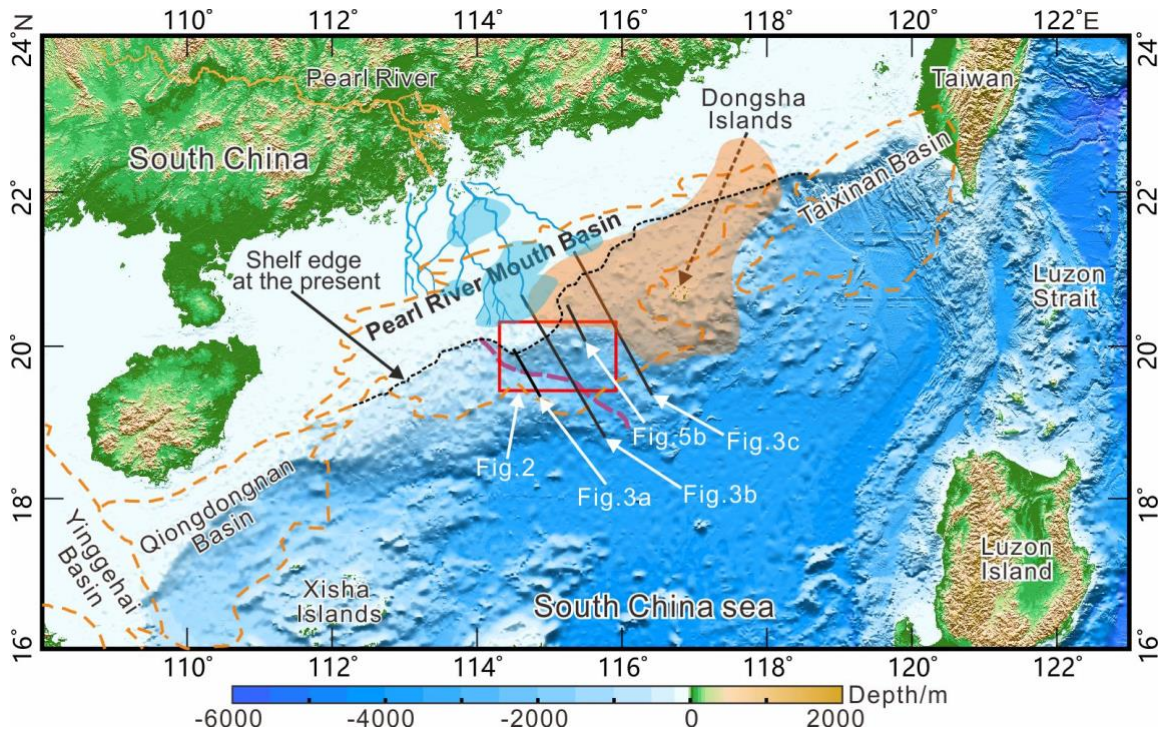
784 sediment waves in submarine canyons since the Penultimate Glacial Maximum (ca. 140 ka), northern South China
785 Sea margin. *Marine and Petroleum Geology* 134, 105381. <https://doi.org/10.1016/j.marpetgeo.2021.105381>.

786 Zhou, W., Wang, Y., Gao, X., Zhu, W., Xu, Q., Xu, S., Cao, J., Wu, J., 2015. Architecture, evolution history and
787 controlling factors of the Baiyun submarine canyon system from the middle Miocene to Quaternary in the Pearl
788 River Mouth Basin, northern South China Sea. *Marine and Petroleum Geology* 67, 389-407.
789 <https://doi.org/10.1016/j.marpetgeo.2015.05.015>.

790 Zhu, M.Z., Graham, S., Pang, X., McHargue, T., 2010. Characteristics of migrating submarine canyons from the
791 middle Miocene to present: Implications for paleoceanographic circulation, northern South China Sea. *Marine and*
792 *Petroleum Geology* 27, 307-319. <https://doi.org/10.1016/j.marpetgeo.2009.05.005>.

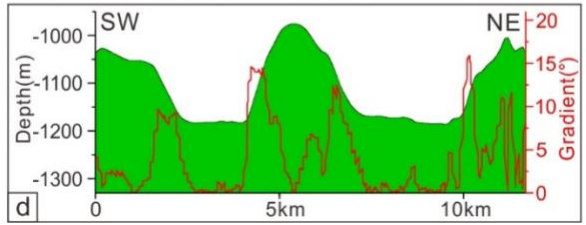
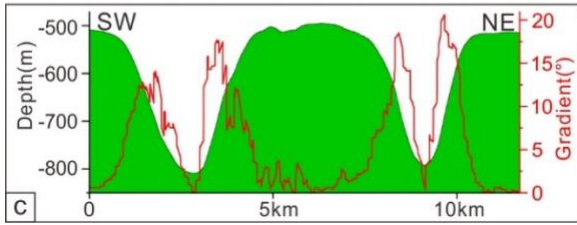
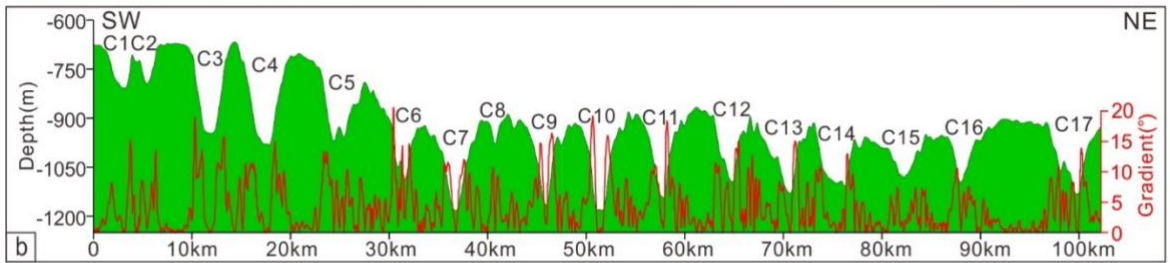
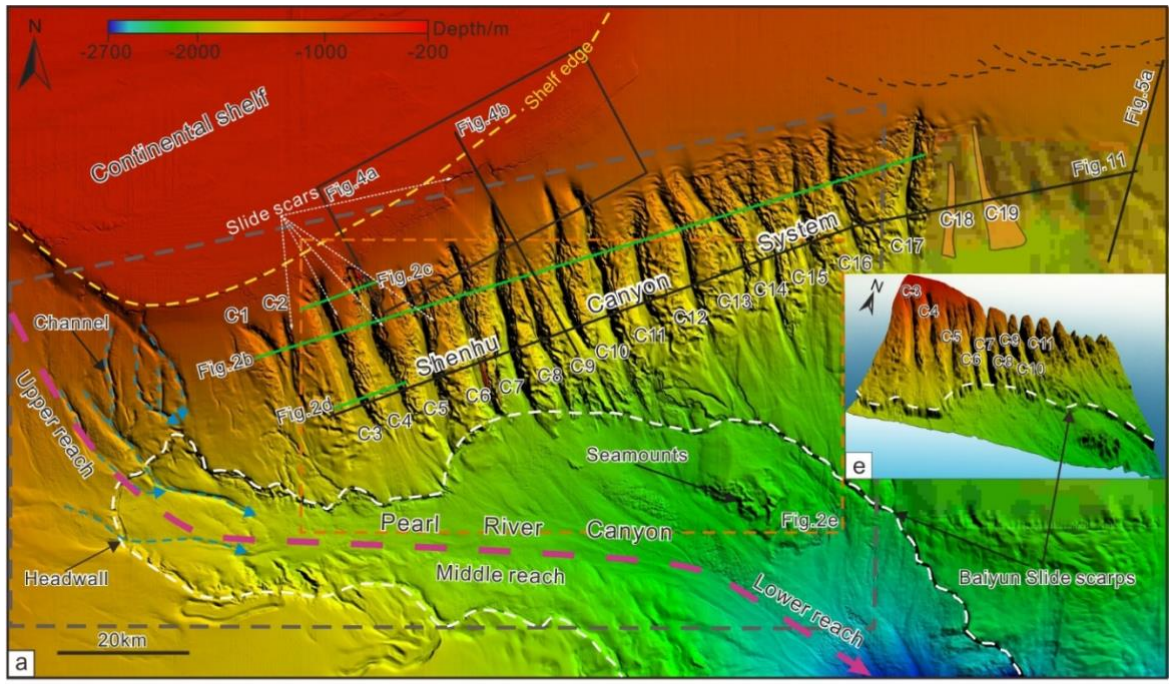
793 Zhu, W.L., Huang, B.J., Mi, L.J., Wilkins, R.W.T., Fu, N., Xiao, X.M., 2009. Geochemistry, origin, and deep-water
794 exploration potential of natural gases in the Pearl River Mouth and Qiongdongnan basins, South China Sea. *Aapg*
795 *Bulletin* 93, 741-761. <https://doi.org/10.1306/02170908099>.

796 Zhuo, H.T., Wang, Y.M., Sun, Z., Wang, Y., Xu, Q., Hou, P.F., Wang, X.X., Zhao, Z.X., Zhou, W., Xu, S., 2019.
797 Along-strike variability in shelf-margin morphology and accretion pattern: An example from the northern margin
798 of the South China Sea. *Basin Research* 31, 431-460. <https://doi.org/10.1111/bre.12329>.



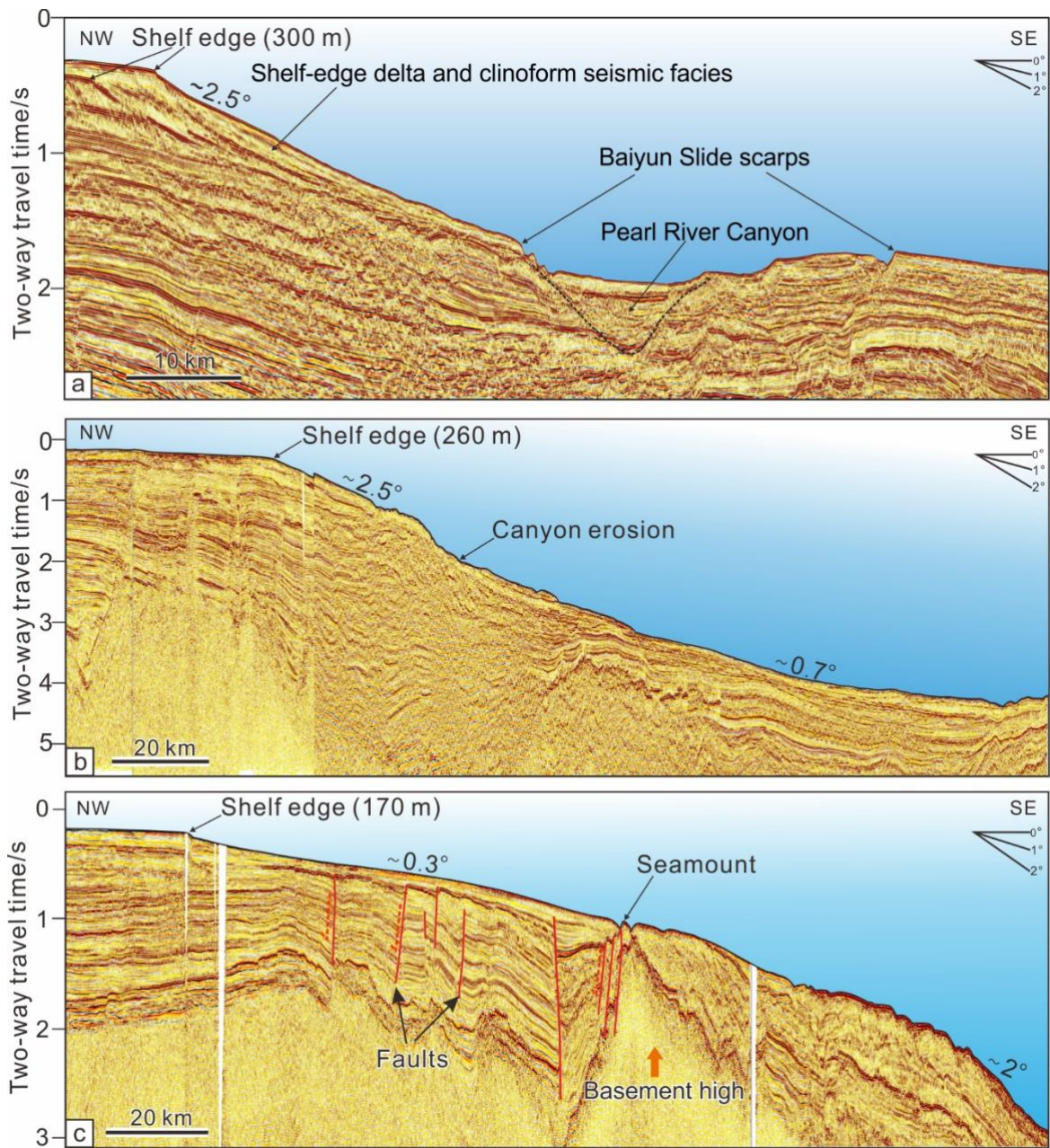
800

801 **Figure 1**



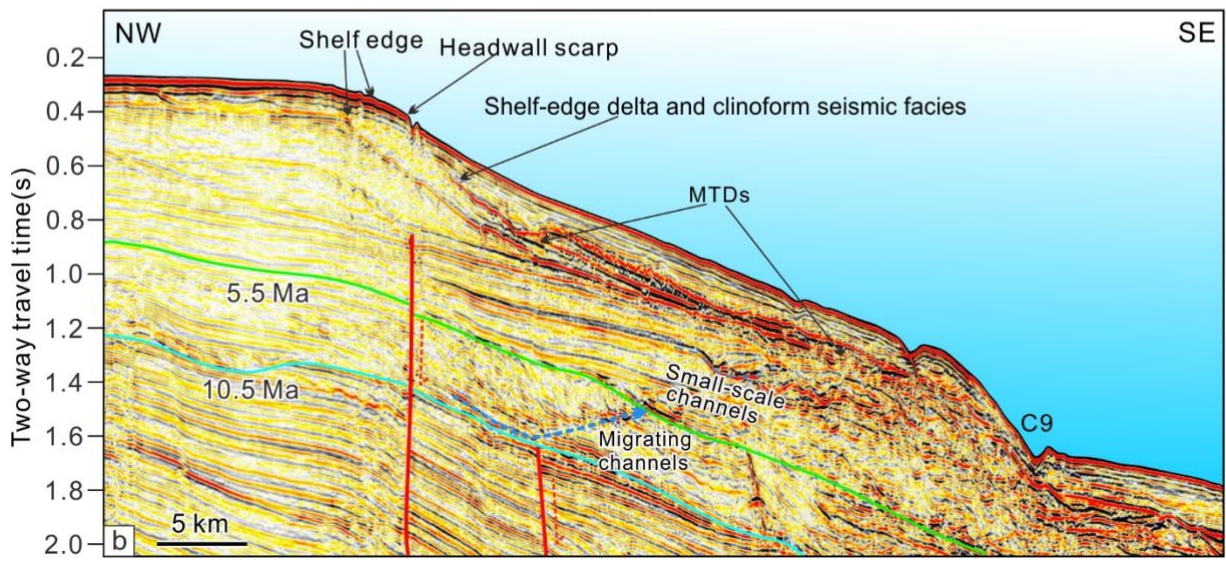
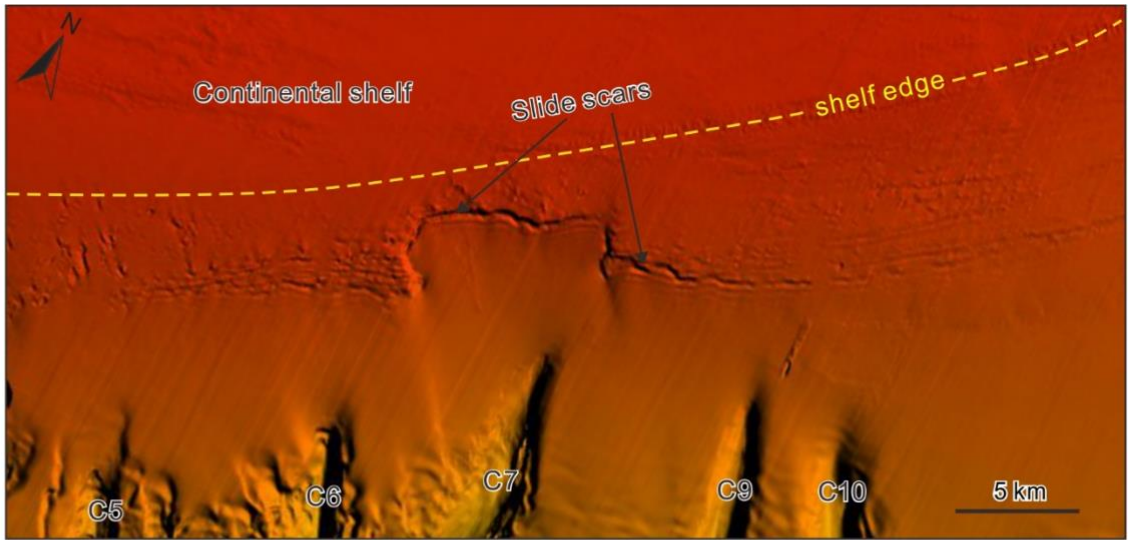
802

803 Figure 2



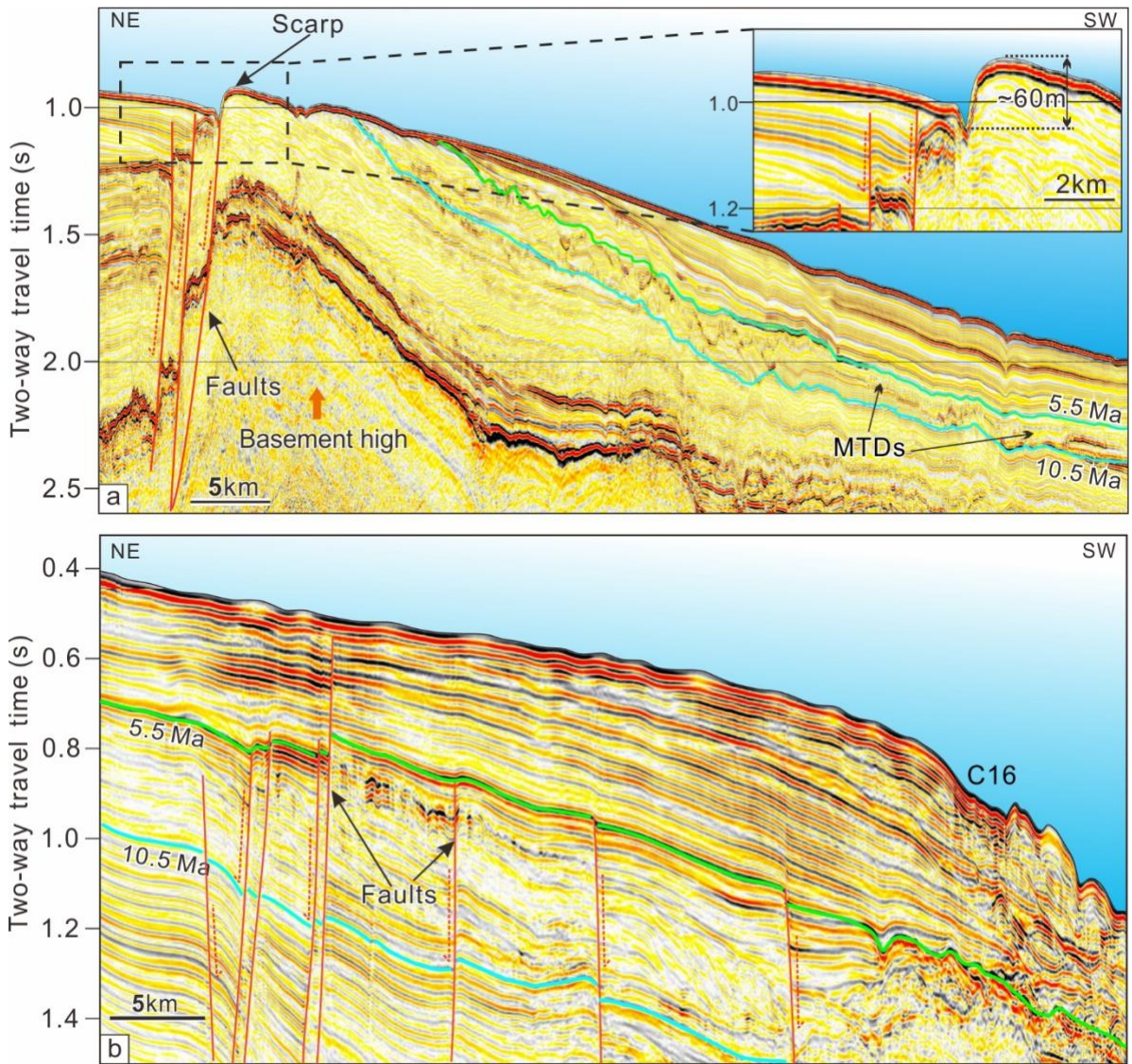
804

805 Figure 3



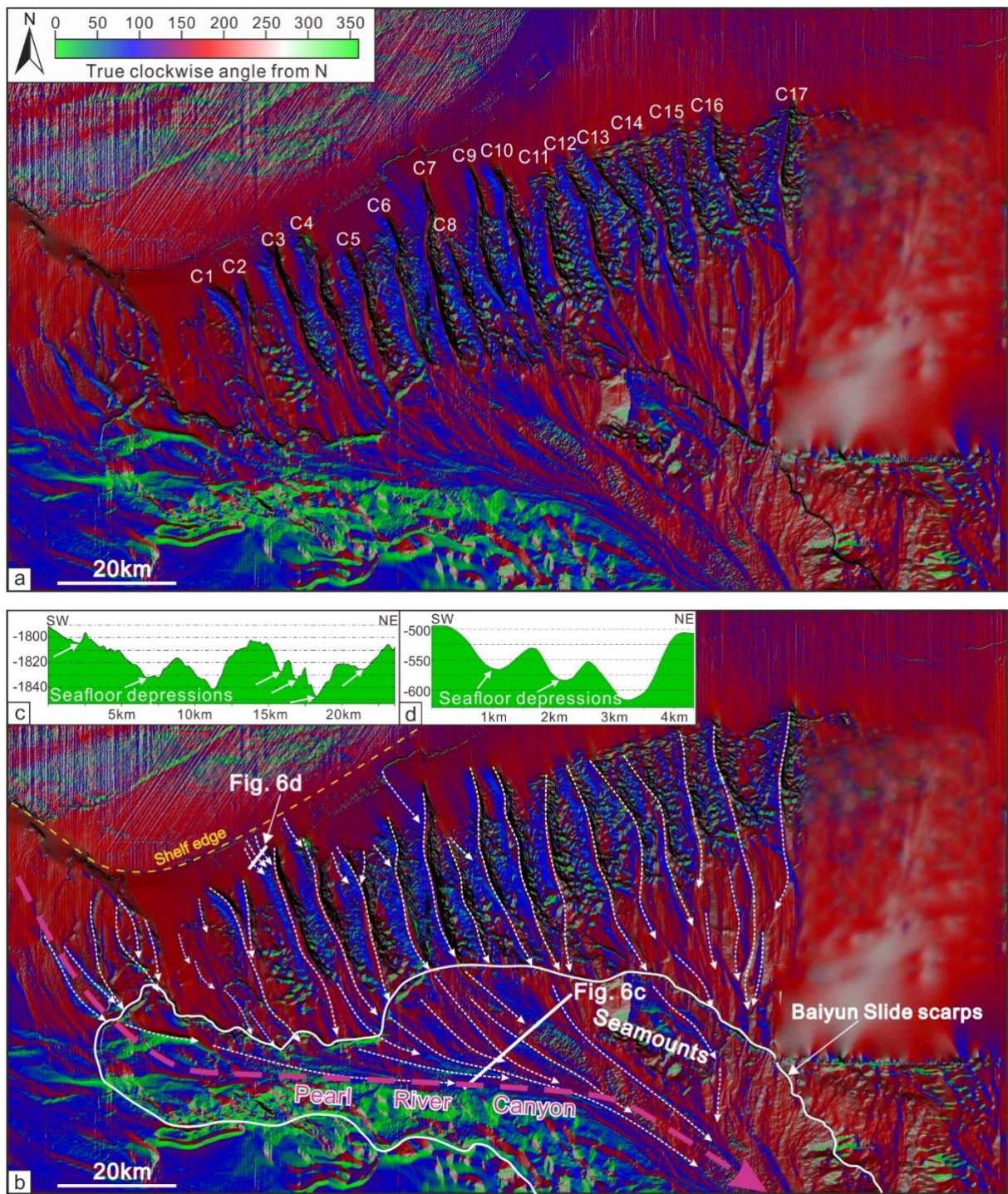
806

807 Figure 4



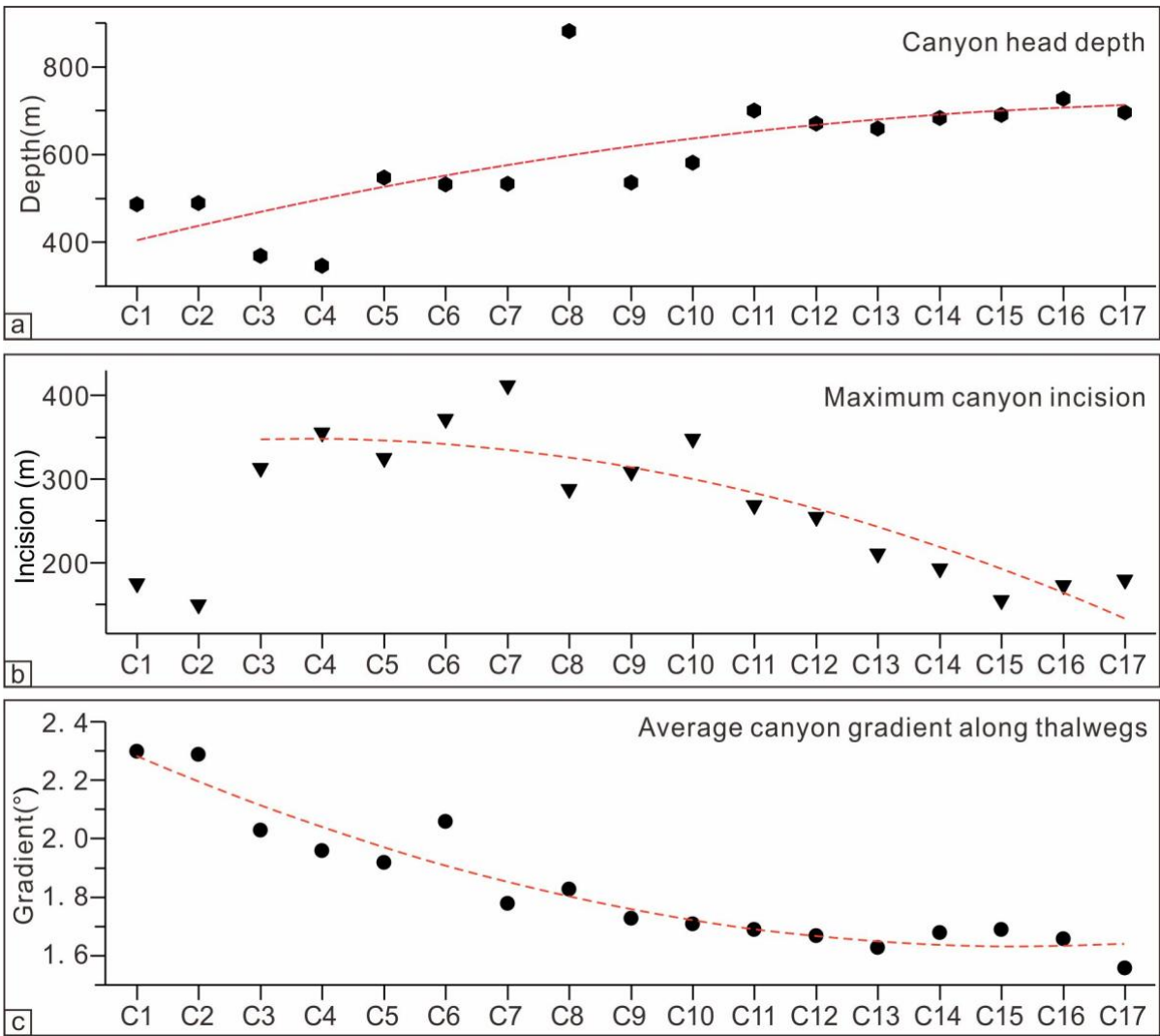
808

809 Figure 5



810

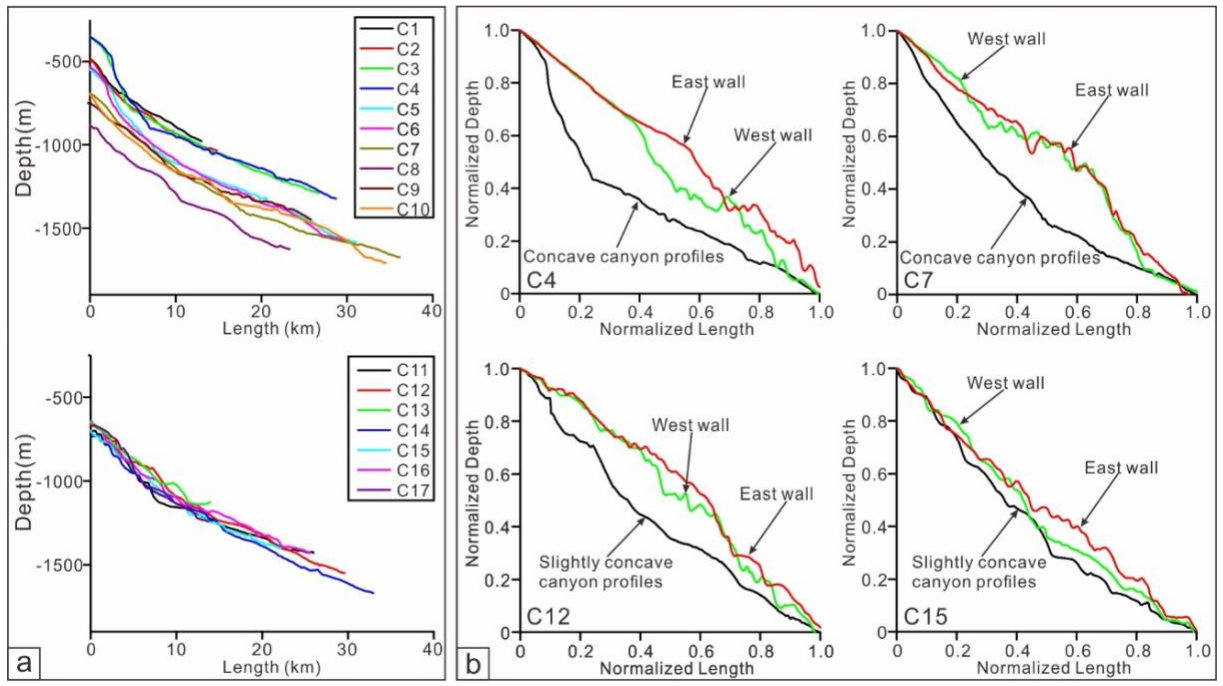
811 Figure 6



812

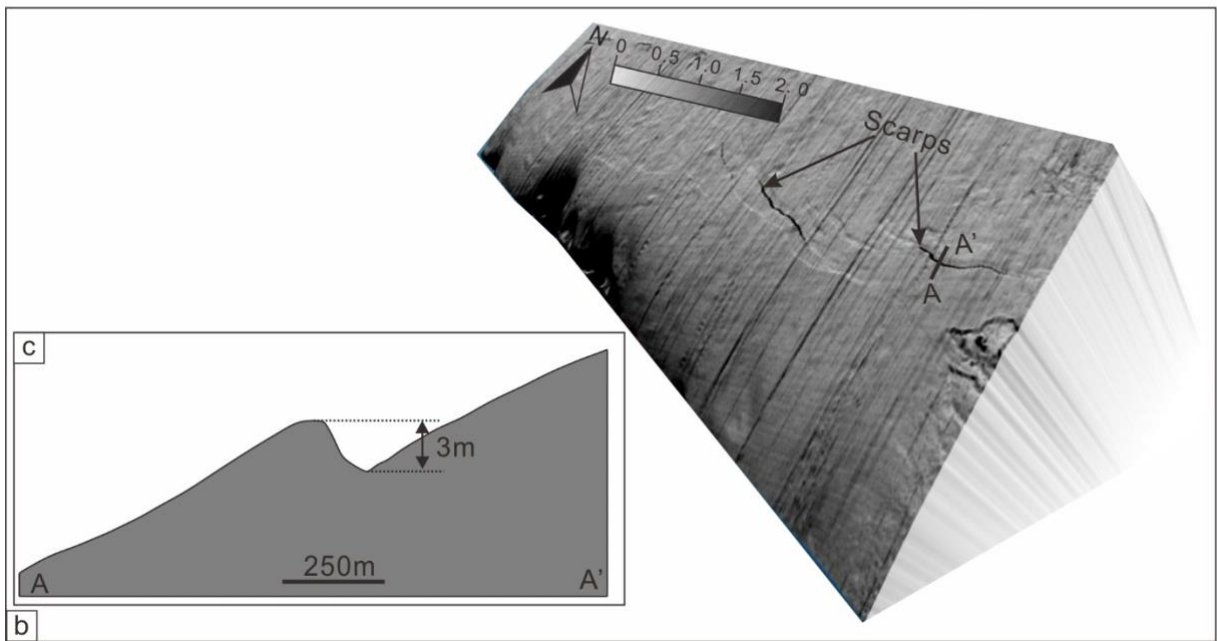
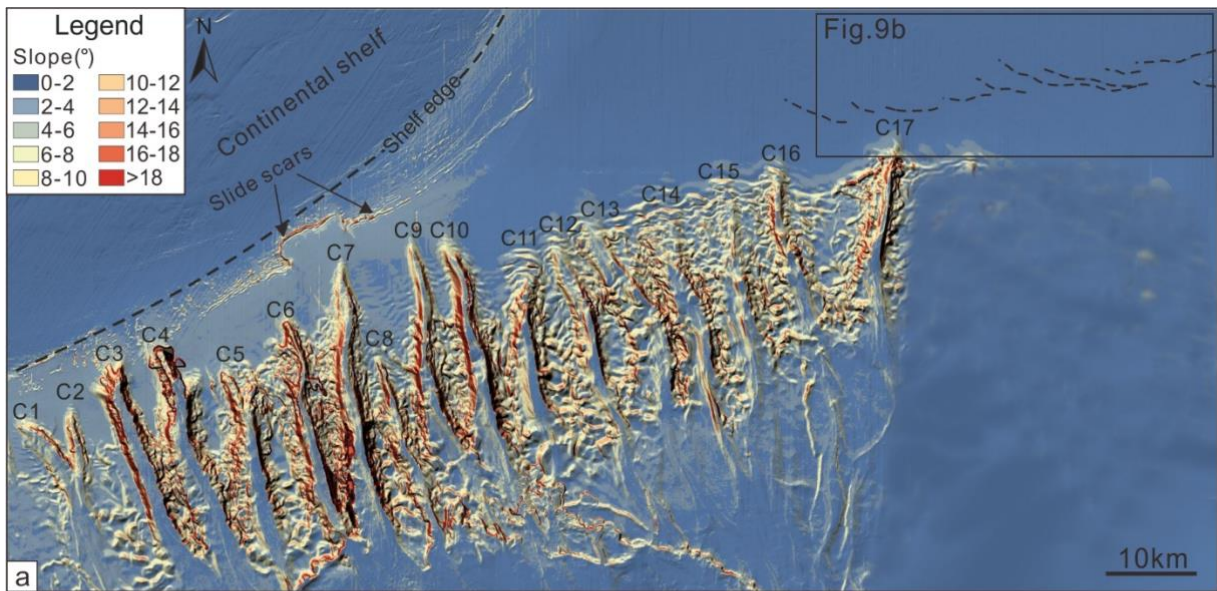
813 Figure 7

814



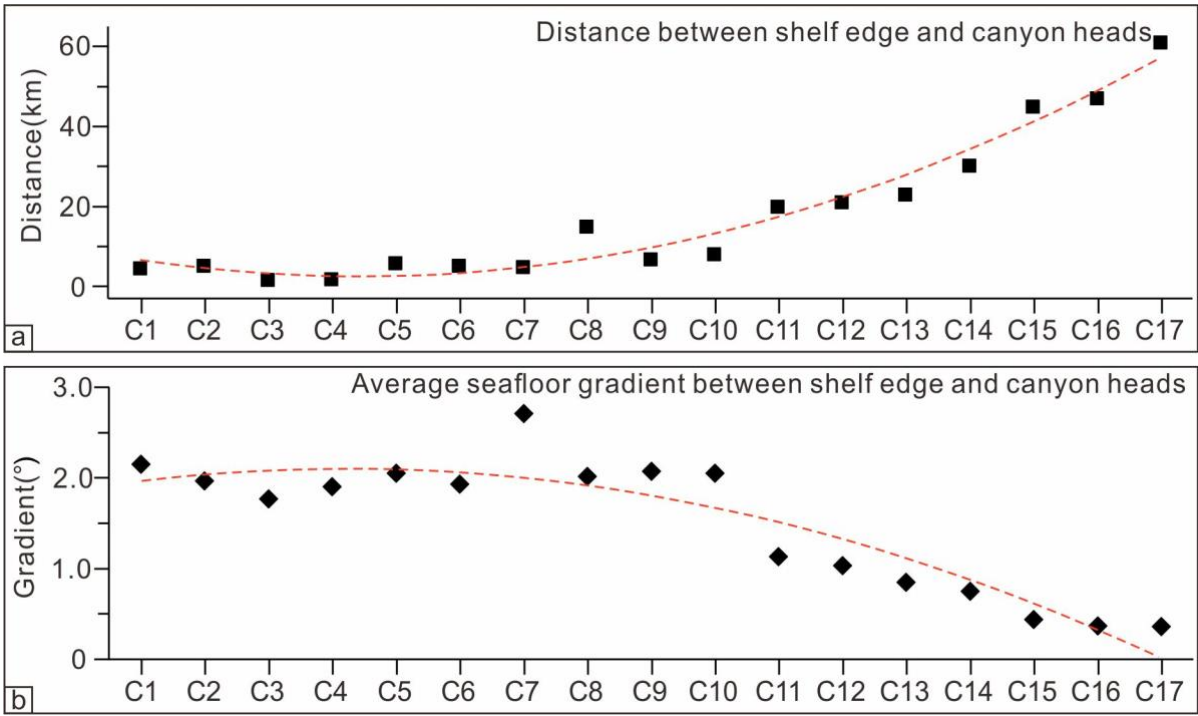
815

816 Figure 8



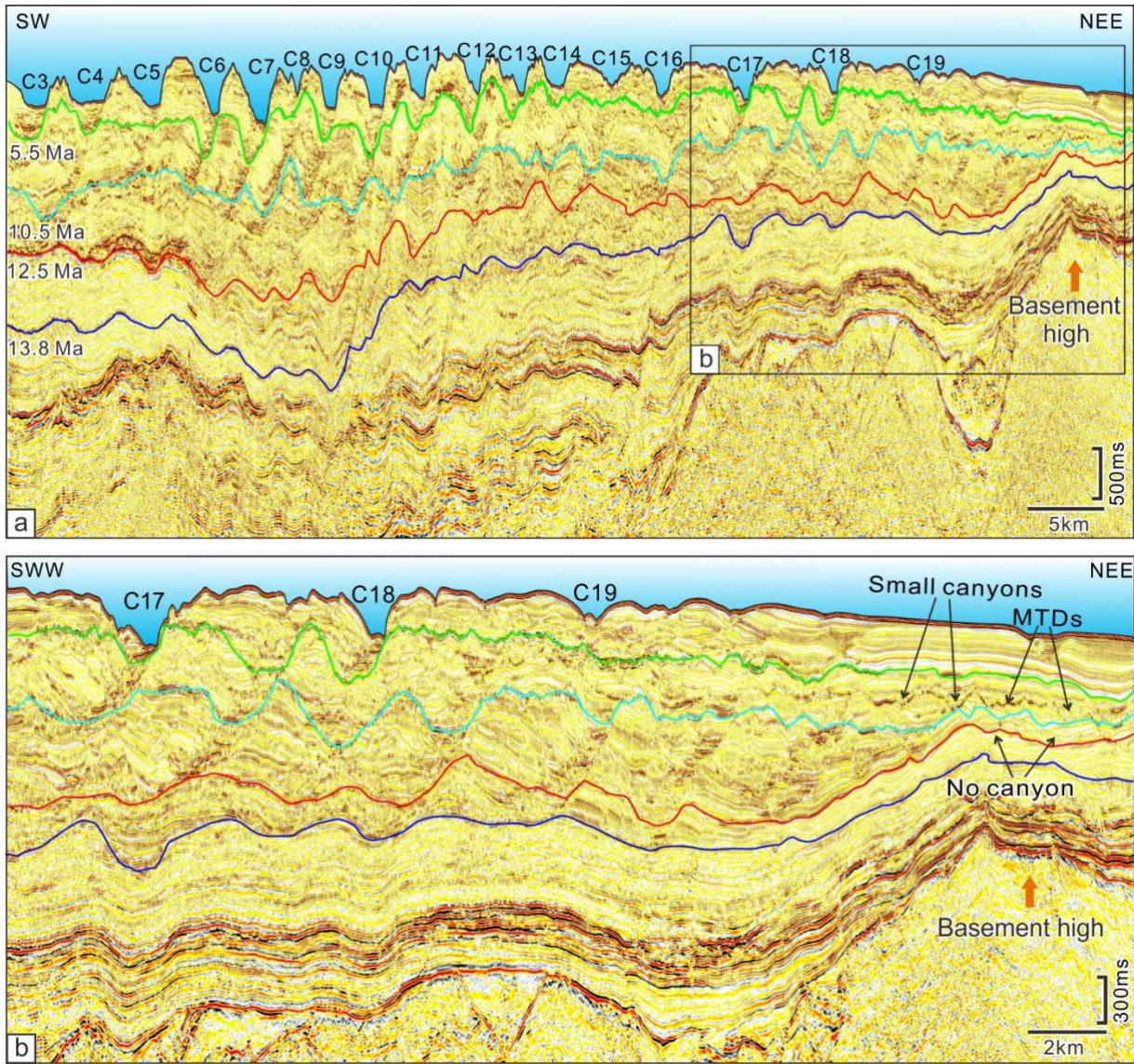
817

818 Figure 9



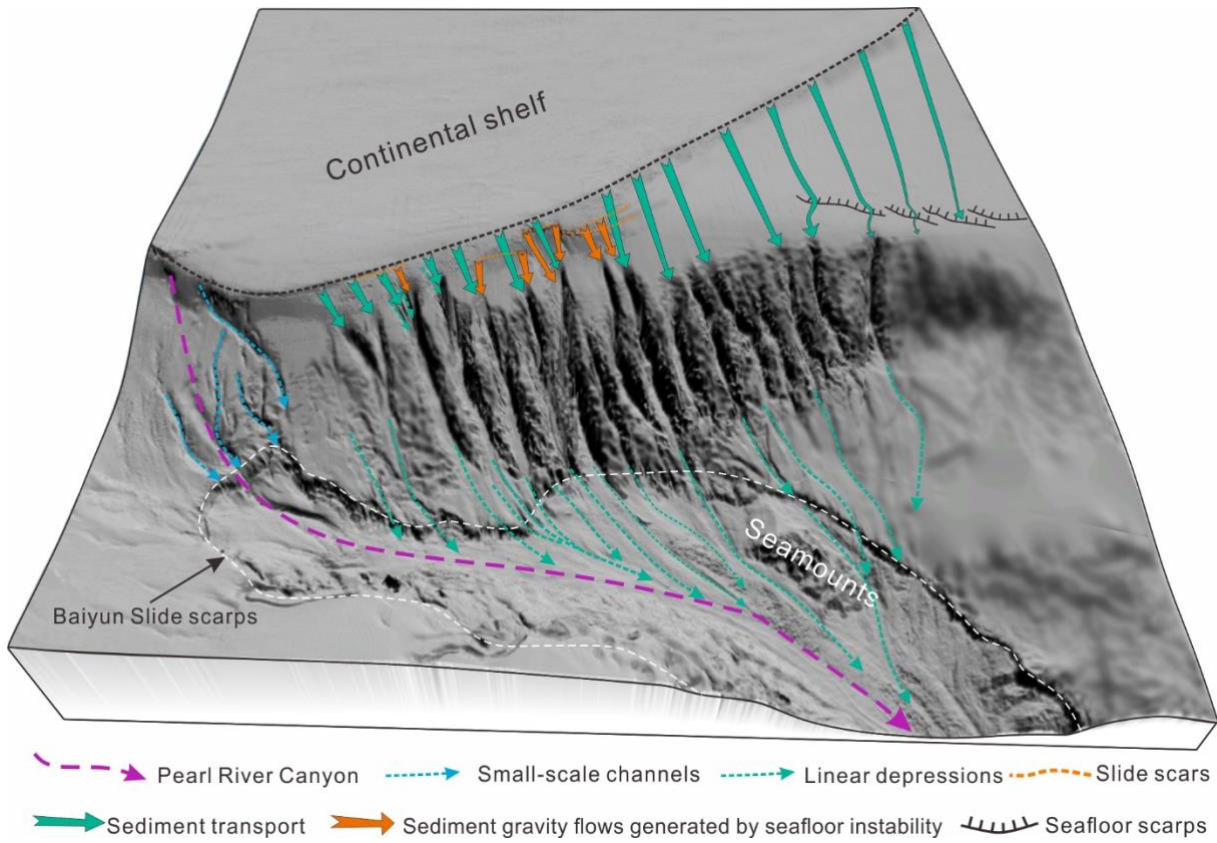
819

820 Figure 10



821

822 Figure 11



823

824 Figure 12

825

826

827

828

829

830

831

832

833

834

835

836

837 **Table**

C	HD (m)	TD (m)	L (km)	SL (km)	S	MI (m)	CGr (°)	Az	D (km)	SGr (°)
1	487	977	13.0	12.2	1.06	175	2.30	144	4.5	2.15
2	490	1050	14.8	12.7	1.17	150	2.29	169	5.1	1.97
3	370	1290	26.7	26.5	1.01	313	2.03	157	1.6	1.77
4	350	1323	28.7	28.5	1.01	356	1.96	157	1.8	1.90
5	547	1583	31.0	30.8	1.01	325	1.92	162	5.8	2.05
6	532	1575	29.9	29.0	1.03	372	2.06	161	5.1	1.93
7	533	1675	36.2	35.3	1.03	412	1.78	164	4.9	2.71
8	880	1626	23.4	23.2	1.01	288	1.83	160	15.0	2.02
9	536	1450	25.9	25.4	1.02	309	1.73	163	6.8	2.07
10	582	1453	26.2	25.8	1.02	348	1.71	168	8.0	2.05
11	700	1550	29.5	29.2	1.01	270	1.69	158	20.0	1.13
12	671	1401	26.7	25.8	1.03	255	1.67	153	21.0	1.03
13	660	1669	33.5	33.1	1.01	211	1.63	159	23.0	0.85
14	683	1402	22.5	22.3	1.01	193	1.68	169	30.2	0.75
15	691	1429	25.5	25.1	1.01	155	1.69	166	45.0	0.44
16	730	1428	23.8	23.4	1.02	173	1.66	161	47.0	0.37
17	696	1413	22.5	22.3	1.01	180	1.56	180	61.0	0.36

838 **Table 1**